

UNCLASSIFIED ~~RESTRICTED~~

COPY NO. 6  
RM No. E8A27-7-1

8 JUN 1948



# RESEARCH MEMORANDUM

ICE PROTECTION OF TURBOJET ENGINES  
BY INERTIA SEPARATION OF WATER  
I - ALTERNATE -DUCT SYSTEM

By Uwe von Glahn

Flight Propulsion Research Laboratory  
Cleveland, Ohio

CLASSIFICATION CANCELLED

Authority J. W. Crawley Date 12/14/53

By QH-1-11-54 Sec no 23  
RF 1966

CLASSIFIED DOCUMENT

This document contains classified information affecting the National Defense of the United States within the meaning of the Espionage Act, USC 5031 and 5041. Its transmission or the revelation of its contents in any manner to an unauthorized person is prohibited by law. Information so classified may be imparted only to persons in the military and naval services of the United States, appropriate civilian officers and employees of the Federal Government who have a legitimate interest therein, and to United States citizens of known loyalty and discretion who of necessity must be informed thereof.

TECHNICAL  
EDITING  
WAIVED

NATIONAL ADVISORY COMMITTEE  
FOR AERONAUTICS

WASHINGTON  
May 28, 1948

UNCLASSIFIED

~~RESTRICTED~~

NACA LIBRARY  
LANGLEY MEMORIAL AERONAUTICAL  
LABORATORY  
Langley Field, Va.



UNCLASSIFIED

NACA RM No. E5A27

NATIONAL ADVISORY COMMITTEE FOR AERONAUTICS

RESEARCH MEMORANDUM

ICE PROTECTION OF TURBOJET ENGINES BY INERTIA SEPARATION OF WATER

I - ALTERNATE-DUCT SYSTEM

By Uwe von Glahn

SUMMARY

The results of a preliminary investigation of internal water-inertia separation inlets designed to prevent automatically the entrance of large quantities of water into a turbojet engine in icing conditions are presented. A simplified analytical approach to the design of internal water-inertia separation inlets is included. The analysis is applied specifically to the model investigated.

The results show that to be effective in separating the free water from the air stream in order to prevent screen and stator-blade icing, an inlet of this type had a 75-percent ram-pressure recovery at the design inlet-velocity ratio in an icing condition. For normal nonicing operation, the ram-pressure recovery is comparable to a direct-ram installation. The ram-pressure recovery and the circumferential uniformity of the mass flow in the inlets was relatively independent of angle of attack.

INTRODUCTION

The axial-flow turbojet engine is subject to impact icing of exposed frontal surfaces during ground operation and in any flight condition during which kinetic heating is insufficient to maintain above freezing the temperatures of the duct lips, inlet walls, screens, accessory housing, and stator blades. At take-off and climb the least kinetic heating occurs, whereas the greatest quantity of air and water is drawn through the engine; icing of the inlet components is expected to be most rapid under these conditions.

It is pointed out in reference 1 that the elimination of free water from induction systems at its source is an effective means of preventing impact icing. The design for a nonicing turbojet-engine inlet must include the following criterions:

~~UNCLASSIFIED~~  
UNCLASSIFIED

1. The initial rate of water intake must be reduced to a minimum.
2. Ram-pressure recovery must be maintained as high as possible in both icing and nonicing conditions in order not to affect the engine performance.
3. The inlet must be automatic in operation throughout an icing condition.

An investigation was conducted at the NACA Cleveland laboratory in order to develop an automatic, ice-free inlet. The investigation of automatically protected inlets for axial-flow turbojet engines was divided into three categories. The first part was confined to a study of single-entrance internal water-inertia separation inlets containing two internal concentric ducts; the next part consisted of an investigation of a water-inertia separation inlet with a single internal passage; and the last part was an investigation of the icing characteristics of annular submerged-nose inlets. A discussion of the first part of the investigation is presented herein.

A proposed design (fig. 1) to eliminate water droplets from the air by inertia separation inside a nacelle consists of a single inlet, a main duct for nonicing conditions, and an alternate duct with a sharply curved inlet through which air with greatly reduced quantities of water droplets can freely pass to the engine when the screen in the main duct becomes blocked with ice. In some icing conditions, this type of inlet will not provide icing protection for continuous operations, inasmuch as the operation time is limited by the location of the ice formations in the duct, which in turn depends primarily on the liquid-water content of the air, the droplet size, and the airspeed. When above-freezing temperatures are encountered, the ice in the main duct melts and the water may be harmlessly drained off through the engine or special drainage facilities may be provided as required.

The design of a water-inertia separation induction system primarily depends upon four configuration variables shown in figure 1; namely, the nacelle-inlet shape, the alternate-inlet gap, the radial offset of the duct-splitter ring above the nacelle-inlet opening, and the curvature of the duct surfaces. The greater the radial offset and the smaller the gap, the less tendency there will be for water droplets to enter the duct; the ram-pressure recovery, however, must also be considered in the induction system and it is this consideration that will principally influence the design of the duct members.

006

The consideration of good ram-pressure recovery requires that all surfaces be as gradually curved and smooth as possible. This requirement is in direct contrast to the requirements for a good water-inertia separation design, which requires sharply curved surfaces for effective water separation. A simplified, approximate analytical method, which is directly applicable to the designs investigated, is presented in appendix A. This analysis can be extended to all types of inertia-separation design within the limitations of the assumptions.

With these conditions in mind, aerodynamic and preliminary icing studies were conducted in the NACA Cleveland icing research tunnel on various configurations of a concentric duct-type water-separating inlet for use with axial-flow turbojet engines.

### SYMBOLS

The following symbols are used in this report:

- a droplet radius, microns
- C body-shape dimensions, feet
- F net thrust of jet, pounds
- G alternate-duct inlet gap, inches
- g acceleration due to gravity, feet per second per second
- K dimensionless droplet inertia parameter
- H total pressure with reference to test chamber, pounds per square foot
- h theoretical radial offset of duct-splitter ring, inches
- h' experimental radial offset of duct-splitter ring, inches
- L maximum cross-sectional height of duct at any section, inches
- l distance from outer duct wall to total-pressure tubes, inches
- M Mach number
- P absolute total pressure of air stream, pounds per square foot
- $P_0$  static pressure of free air stream, pounds per square foot

p	surface static pressure on model, pounds per square foot
q	dynamic pressure of air stream, pounds per square foot
R	alternate-duct-inlet turning radius, inches
$R_d$	Reynolds number based on nacelle diameter
$r_x$	radius to any streamline from center line of nacelle, inches
$r_l$	nacelle-inlet radius, inches
S	pressure coefficient $\left[ 1 - \left( \frac{p - p_0}{q_0} \right) \right]$
T	total temperature of free air stream, °F
V	indicated airspeed, miles per hour
w	weight flow through model, pounds per second
$\alpha$	angle of attack of nacelle, degrees
$\gamma$	ratio of specific heats
$\eta$	ram-pressure recovery $\left[ 1 - \left( \frac{H_0 - H_2}{q_0} \right) \right]$
$\theta$	alternate-inlet turning angle, degrees
$\rho$	air density, slugs per cubic foot
$\phi$	dimensionless droplet parameter

## Subscripts:

av	average
0	free stream
1	nacelle inlet
2	compressor inlet
3	turbine outlet
f	full scale

j jet  
m model  
max maximum

## APPARATUS AND INSTRUMENTATION

The internal water-inertia separation nacelle investigated is shown in figure 2. All inlet models were constructed of wood and had a 21-inch maximum diameter, corresponding to the half-scale dimensions of an axial-flow turbojet engine having an 11-stage compressor, 8 cylindrical burners, a single-stage turbine, and rated at 4000-pound static thrust at sea level. The design of the external contour of the nacelle was based on reference 2. The design inlet-velocity ratio was determined for a free-stream velocity of 550 miles per hour and a maximum air flow of 19.6 pounds per second at an altitude of 40,000 feet.

The models consisted of inlets designed to provide two concentric annular ducts separated by a duct-splitter ring (fig. 3). The nose inlets were mounted on a circular afterbody that was supported at the tunnel center line by a vertical streamlined strut. The area of the duct section behind the parting line of the inlet and the afterbody was equivalent to the compressor-inlet section of a typical axial-flow turbojet engine. The duct outlet was located at the tail section of the body and was provided with a remotely controlled tail cone for varying the outlet area and hence the mass flow through the nacelle. An additional diffuser cone mounted on the tail section of the model was used to obtain high values of inlet-velocity ratio.

The angle of attack of the model was varied by yawing the model in a horizontal plane. The top and the bottom of the nacelle thus corresponded to the horizontal axis of a typical nacelle on an airplane. The angle of attack was determined by an indexing device on the tunnel turntable to which the model was secured.

A screen consisting of concentric streamlined wires was installed in the main air passage, whereas a screen constructed of round wires was located in the alternate air passage. The wires in the main duct were 0.192 inch in chord length and 0.048 inch in thickness, with a center line spacing equal to 0.187 inch. The center line spacing of the wires which were 0.0625 inch in diameter, in the alternate duct was 0.25 inch.

Hatches were so located in the sides of the model that ice formations in the alternate duct could be inspected and the alternate-duct screen could be photographed.

A seven-tube total-pressure rake was mounted in the nacelle-nose section at the rear end of the straight portion of the duct. The rake was used to determine the losses in the inlet due to flow separation at the nacelle nose at angles of attack. In the compressor-inlet plane, a series of total-pressure rakes and static-pressure taps were located and used in order to determine the radial profiles of velocity, mass flow, and ram-pressure recovery. Nine-tube unheated total-pressure rakes were used for aerodynamic runs, whereas six-tube heated total-pressure rakes were used during icing. The rakes were circumferentially spaced about the compressor-inlet section so as to determine the aerodynamic effects of angle of attack on the inlet performance. Whenever possible, total-pressure and static-pressure measurements were also determined in the alternate passage by four-tube total-head rakes and static taps.

The nose inlets were provided with plastic surface-pressure belts located so as to prevent mutual interference and maintain a minimum local reduction in area. The belts were used to obtain measurements of pressure distribution about the curved parts of the duct wall and the duct-splitter ring at angles of attack in nonicing conditions.

Pressure readings were photographically recorded from multiple-tube manometers located in the test chamber.

### CONFIGURATIONS

Combinations of four nacelle-nose designs designated N-1 to N-4 and seven types of duct-splitter ring designated A-1 to A-7 were investigated. All nose designs were investigated as a direct-ram inlet A-0 in order to provide a basis of comparison for the inertia-separation inlets. Coordinates for all inlets with reference to the nacelle nose N-1 in the direction of the X axis and the nacelle center line in the direction of the Y axis are given in tables I to III.

Direct-ram inlet. - The direct-ram inlet A-0 consisted of blocking off and fairing the alternate-duct inlet and outlet so that a single duct was obtained. Duct-splitter-ring configuration A-2 (subsequently described) was arbitrarily chosen for the direct-ram-inlet designs. Cross sections of the nacelle-nose

sections are presented in figure 4. The original nacelle nose N-1, with a design inlet-velocity ratio of 0.77, was based on the results obtained in reference 2 and was used during most of the investigation. The second nacelle nose N-2 consisted of nacelle nose N-1 arbitrarily redesigned to provide a faired inlet with a larger leading-edge radius to prevent the separation of the entering air from the nacelle surface. In an effort to improve further the nacelle nose, a converging nose inlet N-3 was designed. The design inlet-velocity ratio for this inlet was 0.65 and increased to 0.77 just ahead of the alternate-duct inlet. Nacelle nose N-4 was also a converging design with a design inlet-velocity ratio of 0.60 and an effective velocity ratio ahead of the alternate-duct inlet of 0.63. The purpose of the N-4 nose was to decrease the diffusion losses from the inlet section to the region surrounding the accessory housing or main duct. Both noses N-3 and N-4 were investigated with alternate-duct inlet turning radii of 2 and 3 inches.

Duct-splitter rings. - Graphs of the cross-sectional duct areas with the seven types of duct-splitter ring investigated are shown in figure 5. The flow path shown on the area graphs is the distance along the duct center line that the air must traverse from the nacelle inlet to the compressor inlet.

The first configuration A-1 is shown in figure 5(a). The alternate duct had an approximately constant area extending from the inlet of the alternate duct to the end of the elbow. From the elbow aft to the joining of the two concentric ducts, the area increased until at the point of union the areas of the two ducts were approximately equal; each duct was capable of easily handling the required engine air flow. The purpose of this design was to determine the effectiveness of water-inertia separation with a configuration having nearly maximum inertia-separation characteristics.

The second configuration A-2 was designed to obtain good aerodynamic characteristics of the alternate duct at the expense of inertia-separation qualities. In this design, a large inlet area was provided for the alternate duct and diffusion occurred from the inlet to the end of the elbow. Very little diffusion occurred from aft of the elbow to the point of union of the two ducts, as shown in figure 5(b).

Configuration A-3 was designed to incorporate good aerodynamic characteristics as well as improved inertia-separation characteristics. The alternate-duct inlet was large in area but was well offset with respect to the nose-inlet duct surface, as shown in figure 5(c). The area of the two ducts was approximately equal;



each duct was capable of handling independently the required engine air flow at relatively low duct velocities, thus reducing the pressure losses. The accessory housing was moved 4 inches forward from its original position.

Configuration A-4, a variation of configuration A-2, was investigated to determine whether good aerodynamic characteristics might be achieved with the nacelle wall faired smoothly and the duct-splitter ring moved forward to decrease the inlet gap and to obtain improved water-inertia separation. The remainder of the configuration (fig. 5(d)) was the same as design A-2.

Configuration A-5 consisted of the faired nacelle wall used in configuration A-4 and a duct-splitter ring similar to that of A-3 but utilizing a narrower inlet gap, as shown in figure 5(e).

In configuration A-6 (fig. 5(f)), an effort was made to increase the ram-pressure recovery for the alternate duct by moving the duct-splitter ring used in A-1 rearward  $3/8$  inch. This change resulted in an increase in the alternate-duct-inlet area, but maintained the sharp curvature of the inlet elbow.

The final configuration A-7 was designed with a constant-area duct from the nacelle inlet back to the downstream end of the alternate-duct elbow. Aft of the elbow the area variation was similar to design A-1, as shown in figure 5(g).

Radial offset of the duct-splitter rings  $h'$  and alternate-inlet gap  $G$  are presented in the following table:

Configuration	$h'$ (in.)	$G$ (in.)
A-1	0.75	0.65
A-2	.65	1.90
A-3	1.85	2.50
A-4	.65	.90
A-5	1.85	1.12
A-6	.75	1.00
A-7	1.05	1.25

#### PROCEDURE

The investigation was conducted in the 6- by 9-foot high-speed test section of the NACA Cleveland icing research tunnel at a tunnel velocity of approximately 260 to 280 miles per hour.

The aerodynamic investigation was made with the screens removed, with the model at angles of attack of  $0^\circ$ ,  $4^\circ$ , and  $8^\circ$ , and at inlet-velocity ratios varying from 0.25 to 0.82. The model was also investigated for the same range of conditions with air flowing only through the alternate duct by blocking the main duct with a plate at the screen location in order to simulate an icing-flight condition. The mass flow through the model was determined by two heated total-head rakes and heated static-pressure taps located in the tail section of the model. Investigations were also made with the compressor screens in place.

A series of preliminary icing investigations of the configurations were made at the design inlet-velocity ratio in order to determine icing characteristics of the inlets. The icing experiments were conducted at a tunnel velocity of 260 miles per hour and at an angle of attack of  $0^\circ$ . Some configurations were also studied at an angle of attack of  $8^\circ$  in order to determine the effect of angle of attack on the ice distributions in the ducts. The spray equipment used for icing the configurations consisted of air-atomizing water spray nozzles so mounted that the model could be operated at various angles of attack and yet maintain a relatively uniform water concentration in a plane passing through the top and the bottom of the nacelle. The water concentration deficiency at the sides of the model was unimportant because the purpose of the investigations was to obtain evidence of where ice formed on the model surfaces rather than to conduct a complete icing investigation.

The droplet size and water concentration were determined by rotating cylinders. The droplet size used was approximately 12 to 15 microns by volume maximum. Water concentrations from 0.5 to 3.5 grams per cubic meter were used in order to obtain rapid and large deposits of ice. The total air temperature for the investigations ranged from  $20^\circ$  to  $28^\circ$  F. The duration of the icing period varied from 10 to 20 minutes; at the end of the period, photographs were taken of the nacelle nose and deflection ring, alternate duct and elbow, and the compressor-inlet screen. The effectiveness of the inertia-separation characteristics of the inlets was determined by the amount of ice on the alternate-duct screen.

#### AERODYNAMIC INVESTIGATION

Surface static-pressure distribution. - Pressure-distribution measurements in terms of the pressure coefficient  $S = \left[ 1 - \left( \frac{p - p_0}{q_0} \right) \right]$

about the nacelle-inlet nose are shown in figure 6. For a velocity ratio  $V_1/V_0$  of 0.70 (fig. 6(b)), the stagnation point was located on the outside of the nose, which resulted in very high velocities about the nose leading edge at angles of attack above 4 degrees. Large total-pressure losses resulted in the nose inlet from flow separation at the bottom inlet surface, as shown in figure 7.

The pressure distribution for a direct-ram installation using nose N-2 (fig. 6(c)) indicates that the stagnation point has been moved more inside the inlet lip at an angle of attack of  $0^\circ$ . This location of the stagnation point resulted in greatly reduced inlet-pressure losses at all angles of attack. Both nacelle noses N-3 and N-4 (figs. 6(d) and 6(e) respectively) indicated the same movement of the stagnation point.

Typical pressure distributions in terms of the pressure coefficient  $S$  along the nacelle surface at the alternate-duct inlet and about the leading edge of the duct-splitter ring are shown in figure 8 for normal operation; these distributions were only obtained for configurations A-1, A-2, and A-3.

With the main duct blocked, the flow about the duct-splitter-ring leading edge on all designs is of relatively high velocity, as shown by configuration A-1, A-2, and A-3 in figure 9. The air, which enters the main duct and is forced out again, must negotiate the curve around the leading edge of the duct-splitter ring; consequently, when the air rounds this point a high velocity exists for a short distance. This velocity condition is inherent in the design and contributes somewhat to a reduced ram-pressure recovery. For configuration A-1, which had a very small alternate-duct cross-sectional area, as shown in the area graph in figure 5(a), extremely high velocities were prevalent in the alternate duct (fig. 9(a)). The high velocity for configuration A-1 was favorable for considerable secondary water-inertia separation in the elbow, as will be shown later.

Ram-pressure recovery. - The ram-pressure recovery  $\eta$  was calculated as  $\left[ 1 - \left( \frac{H_0 - H_2}{q_0} \right) \right]$ , where the total-pressure difference is the integrated average total-pressure loss at the compressor-inlet section. The integrated average recovery of all the aerodynamic rake stations in the compressor-inlet section was chosen as the configuration ram-pressure-recovery value.

A shift in mass flow (fig. 10) and consequently a decrease in ram-pressure recovery were observed with nose N-1 at high angles of attack because the entering air stalled at the bottom of the

006  
0

nacelle nose and surfaces. The other nacelle-nose sections were not subject to flow separation at the inlet surfaces because of the improved inlet designs.

The ram-pressure recovery for configuration A-0 with four nose designs is shown in figure 11 as a function of inlet-velocity ratio and at an angle of attack of  $0^\circ$ . The results indicate no appreciable difference with the various nose designs. The ram-pressure recovery for nose sections N-2, N-3, and N-4 did not vary more than 1.5 percent at angles of attack up to  $8^\circ$  from the values attained at  $0^\circ$  angle of attack. The inlet-pressure-loss curves for these three sections are at a minimum and do not vary appreciably up to an angle of attack of  $8^\circ$ . Pressure losses were incurred as the air passed over the accessory-housing nose due to the sudden expansion of the air as it passed from the straight inlet section to the much greater area surrounding the accessory housing and to the wakes from the struts supporting the duct-splitter ring. The rough surfaces of the model also contributed to a reduced ram-pressure recovery. Surface roughness can contribute up to 50 percent of the duct-pressure loss (reference 3). Discontinuities and protuberances on the surfaces of the model also considerably increased the ram-pressure losses and affected points of local ice formation.

The variation of ram-pressure recovery with inlet-velocity ratio is shown in figure 12(a) for normal operation without compressor-inlet section screens. No air passes through the alternate duct for normal flight operation, as determined by total- and static-pressure measurements obtained in the rear part of the alternate duct.

With the main duct blocked off, as would be the case for an icing condition, the ram-pressure recovery rapidly decreased with an increase in the inlet-velocity ratio (fig. 12(b)). The configurations having large alternate-duct-inlet gaps and good fairing of contours show a higher recovery than the small-gap designs. The fairing of the alternate-duct elbow also improved the ram-pressure recovery.

Additional aerodynamic investigations were conducted with configuration A-7 and consisted in determining the effect of the redesigned nose sections on the ram-pressure recovery for normal operation and for operation with the main duct blocked. (See fig. 13.) For normal operation (fig. 13(a)), an inlet with a lower design inlet-velocity ratio (nose N-4) will increase the ram-pressure recovery of the system to as much as 87 percent, which is about 12 percent above that obtained with high velocity-ratio inlets (noses N-1, N-2, and N-3). An increase in ram-pressure recovery up to 87 percent with nose N-4 is also observed

when the main duct is blocked off (fig. 13(b)). With a properly designed inlet, a high ram-pressure recovery may be achieved with an internal water-inertia separation inlet that compares favorably with a direct-ram inlet for normal flight operation. The ram-pressure recovery with the main duct blocked is shown to be improved above the values obtained in this investigation with nose N-1 if a well-designed nose inlet is used. The change in nacelle-wall radius from 3 to 2 inches did not affect the aerodynamic performance of the duct system.

The change in total pressure between the alternate-duct total-pressure rakes and the compressor-section rakes was very small, which indicates that the principal ram-pressure loss with the main duct blocked was incurred at the alternate-duct inlet.

The effect of Reynolds number on the ram-pressure recovery is shown in figure 14 for configuration A-4 with the main duct blocked. As the Reynolds number increases, the ram-pressure recovery also increases.

Installation of the round-wire screen ahead of the compressor-inlet section caused a 5- to 10-percent additional loss in recovery.

The effect of ram-pressure recovery on the net thrust obtained with a typical 4000-pound static-thrust turbojet engine calculated by the method in appendix B is shown in figure 15. As engine-pressure ratio increases, the effect of ram-pressure recovery on net thrust decreases. As free-stream Mach number  $M_0$  increases, the effect of high ram-pressure recovery becomes increasingly more important. At a low value of  $M_0$  such as 0.2 (fig. 15(a)), which is representative of take-off conditions, the net thrust is affected very little by as low a ram-pressure recovery as 50 percent. At a cruise condition of  $M_0 = 0.6$  in icing weather, a recovery of only 75 percent will still maintain 91 percent of the net thrust (fig. 15(c)). As ram-pressure recovery is reduced by icing, the engine thrust can be maintained constant by increasing fuel flow until rated engine speed, or maximum allowable tail-pipe temperature, or both are reached.

In general, the effect of ram-pressure recovery on net thrust changes very little with altitude. The results can thus be assumed to be representative of sea-level conditions. For take-off and climb, little engine thrust is lost because of a low ram-pressure recovery, whereas at a cruise condition less than 10 percent of the net thrust would be lost in an icing condition. When the inlet is not iced (normal operation), less than 3 percent of the net thrust need be sacrificed with a good internal water-inertia separation inlet.

900

Velocity distributions. - Typical radial velocity profiles for the compressor-inlet section are shown in figure 16 for normal flight operation at two angles of attack and with no screens ahead of the compressor inlet. The profiles at an inlet-velocity ratio of approximately 0.75 are relatively uniform for all configurations at an angle of attack of  $0^\circ$ ; however, at an angle of attack of  $8^\circ$  for most of the configurations including the direct-ram inlet, the profiles are less uniform. In most cases, the addition of screens in the duct tended to make the velocity profiles more uniform. Decreasing the inlet-velocity ratio did not appreciably change the velocity profile or the magnitude of the percentage variation of the local velocities from the average velocity.

When the main duct was blocked in order to determine the velocity profiles that might be expected in an icing operation, the velocity profiles became relatively nonuniform, even at an angle of attack of  $0^\circ$ , as shown in figure 17. The profile for configuration A-4 had the highest ram-pressure recovery; yet, it also had the largest velocity-profile gradient of all the designs. The profile possibly could be considerably improved with a properly designed screen ahead of the compressor inlet.

For normal flight operation with air passing through the main duct, the mass flow was relatively uniform up to an angle of attack of  $8^\circ$  for all the configurations with noses N-2, N-3, or N-4. The direct-ram configuration with nose N-1 showed a definite tendency toward a shift in mass flow at angles of attack above  $4^\circ$ .

For the flight condition in which air enters the engine through the alternate duct with nose N-1, only configuration A-1 maintained a relatively uniform circumferential mass flow at all angles of attack. Both configurations A-3 and A-5 exhibited such poor stalling and flow-separation characteristics at small angles of attack that, although the angle of attack was decreased to  $0^\circ$ , the stalling characteristics were often impossible to reduce or eliminate. The flow instability was believed to be caused by the small leading-edge radius and the relatively large radial offset of the duct-splitter ring. The results show that the smaller the inlet area or gap, the less the mass flow will shift and the more insensitive the inlet is to air-flow separation at the nacelle nose.

#### ICING INVESTIGATION

Sketches and photographs of typical ice formations are shown in figures 18 to 21. At an angle of attack of  $0^\circ$ , no ice formations of any significance were observed on the inlet surfaces for

noses N-1 and N-2. At lower inlet-velocity ratios, some ice was deposited on the inlet surfaces and decreased the inlet area. Noses N-3 and N-4 exhibited more inlet-surface icing due to a lower inlet-velocity ratio as well as the convergence of the surfaces. The nose designs did not appear to affect the icing characteristics of the alternate duct. At angles of attack, the upper portion of the nacelle-nose inlet surface was subjected to direct water impingement and severe ice formations were observed on the longer icing runs; however, in no case did ice accrete on the duct-splitter ring outer surface aft of the alternate inlet. Main-duct and accessory-housing surfaces became coated with moderate-to-heavy formations of ice.

A description of the icing characteristics of the various inlets follows.

Configuration A-1. - Ice formations on the duct-splitter ring for configuration A-1 (fig. 18(a)) did not extend into the alternate-duct inlet. At an angle of attack of  $8^\circ$ , the ice formations at the top of the nacelle extended into the alternate-duct inlet on the duct-splitter ring  $1/2$  inch up from the bottom of the leading edge of the ring. Severe ice formations of  $3/32$  inch maximum thickness occurred in the alternate-duct elbow as a result of secondary inertia separation. The ice formations did not extend aft of the elbow and the diffusing section in the duct was entirely free of ice. The uniform ice formation around the periphery in the alternate-duct inlet elbow at angles of attack was due to the uniform mass flow. Light frost formations were observed in some instances to coat the screen ahead of the compressor-inlet section but at no time was there sufficient ice on the screen to warrant the descriptive name of light ice or ice traces. Decreasing the mass flow through the model by changing the inlet-velocity ratio from approximately 0.72 to 0.60 did not appear to affect the location or deposition of ice in the alternate duct.

Configuration A-2. - Ice formations on the duct-splitter-ring leading edge extended up into the alternate-duct inlet for  $3/8$  to  $1/2$  inch for configuration A-2. Light icing occurred in the inlet elbow and severe ice formations were observed on the nacelle walls in the alternate duct. The severest icing occurred about  $1\frac{1}{2}$  inches aft of the elbow (fig. 18(b)) where a rough ridge of ice due to model protuberances built up to a  $1/4$  inch thickness. Aft of this ridge, the ice formations tapered off in about 4 inches until only light ice traces remained in the slight bend ahead of the compressor-inlet screen. Medium ice formations were observed on the screen and the screen brackets with slightly heavier deposits of ice near the outer periphery of the screen. The ice formations on the round

wires of the screen were of a pointed sliver type extending upstream as much as 1/16 inch, as shown in figure 18(b).

At an angle of attack of  $8^\circ$  (figs. 19(a) and (b)), the ice formations on the leading edge of the duct-splitter ring extended further into the alternate duct in the top quarter than in the bottom quarter of the nacelle.

Configuration A-3. - For configuration A-3, ice formations on the duct-splitter ring were only observed on the inner surface of the leading edge at an angle of attack of  $0^\circ$  (fig. 18(c)). In the alternate duct, ice formations similar in both magnitude and location to that in configuration A-2 were observed and the screen icing was also the same. Inasmuch as the duct-splitter-ring leading edge was at a greater radial distance from the nacelle center line than the previous configuration, the ice formation on the leading edge did not extend into the alternate-duct inlet because primary separation occurred inboard of the duct-splitter ring.

Configuration A-4. - In general, the icing characteristics of configuration A-4 did not greatly differ from the A-2 configuration (fig. 18(d)). The ice accretions on the duct-splitter ring were confined to the lower side of the deflection ring more than for the A-2 design. The nature of the nacelle-wall fairing in the inlet elbow and extending aft into the alternate duct appeared to augment the ice formations (fig. 20). In general, the heavy ice formations extended about 6 inches aft of the elbow in the duct. Moderate screen icing of the type previously described for configuration A-2 was also present.

Configuration A-5. - The icing characteristics of configuration A-5 (fig. 18(e)) were similar to those of the A-3 design. The flow instability previously described caused erratic icing on the nacelle inlet resulting from the fluctuations in inlet velocity.

Configuration A-6. - In general, the icing characteristics of configuration A-6 (fig. 18(f)) were similar to those of A-1. The icing on the outer surface of the alternate duct extended about 4 inches aft of the inlet elbow. As a result of the larger alternate-inlet gap, a trace of ice was observed on the screen.

Configuration A-7. - Light traces of ice were observed on the wall surface almost the full length of the alternate duct (figs. 18(g) and 21). A light ice formation covered the alternate-duct screen but did not appear to affect the ram-pressure recovery. This configuration appeared to have the best over-all performance of those investigated.



Icing characteristics with both ducts open. - Two icing runs were made with configuration A-7 at an angle of attack of  $0^\circ$  in order to determine the icing characteristics of the main-duct screen and to determine how the transfer of mass flow from the main to the alternate duct affected the ram-pressure recovery. The change in ram-pressure recovery and inlet-velocity ratio with elapsed time for a 20-minute icing run is shown in figure 22. The main-duct screen was almost completely blocked, as shown in figure 23(a). As previously mentioned, the icing sprays used did not uniformly cover the inlet area, which caused eccentric formations of ice on the main-duct screen. The outer periphery of the main-duct screen iced more slowly because of water-deflection effects in the main duct. The alternate-duct screen was covered with a small trace of ice. Moderate ice formations were observed in the alternate-duct elbow and on the nacelle-wall surfaces.

Extrapolation of model icing investigations to full scale. -

If the values of the  $K$  and  $\phi$  parameters (where  $K = f(a^2 V/C)$  and  $\phi = f(\rho^2 VC)$ ) for the model and full-scale nacelle are maintained the same, the icing characteristics of the model will be similar to the icing characteristics of the full-scale nacelle as determined by Langmuir and Blodgett. Each component of a complicated duct system will have its own  $K$  and  $\phi$  values; however, by choosing the most important component for a particular investigation a satisfactory extrapolation to full scale can be attained. The equations of  $K$  and  $\phi$  contain four important variables: velocity, drop diameter, body dimension, and density, which can be varied simultaneously, separately, or in combination.

For the investigation presented, the data were extrapolated from half scale to full scale by holding  $K$  constant and so changing the density or pressure altitude for the full-scale nacelle that  $\phi_m$  for the half-scale model was the same as  $\phi_f$ .

The half-scale model conditions for these investigations thus pertain to full-scale conditions at a pressure altitude of approximately 21,000 feet.

Design recommendations. - Secondary water-inertia separation of droplets in the alternate-duct elbow may limit the operation time in icing conditions unless the surface is locally heated. Local heating of the nacelle leading edge, nose-inlet surfaces, and duct-splitter ring may also be required to maintain maximum efficiency in long encounters with ice. The main-duct screen should be designed to ice much more rapidly than the inlet guide vanes in order to transfer quickly the air flow into the alternate duct and prevent excessive guide-vane icing. If a screen is required in the alternate duct, the screen should be designed for a minimum icing rate.

## SUMMARY OF RESULTS

The investigation showed that for an internal water-inertia separation inlet of two concentric-duct types, the following results were obtained:

1. Automatic ice protection for turbojet engines was accomplished. For the particular installation investigated, inertia-separation ice protection was incorporated in a conventional high-critical Mach number nacelle without increasing the nacelle diameter.
2. Good ice protection for a high inlet-velocity-ratio nacelle was obtained with a ram-pressure recovery of 75 percent, which corresponds to a loss in thrust of 9 percent for a 4000-pound-thrust turbojet engine at a free-stream Mach number of 0.6.
3. In a nonicing condition, the ram-pressure recovery of the system approached that of a single-duct direct-ram inlet.
4. No eccentric flow shifts in the model or additional ram-pressure losses were observed with suitable nose inlets for angles of attack up to  $8^\circ$ .

Flight Propulsion Research Laboratory,  
National Advisory Committee for Aeronautics,  
Cleveland, Ohio.

## APPENDIX A

## ANALYTICAL INERTIA-SEPARATION INLET DESIGN METHOD

For a high critical Mach number nacelle design incorporating a straight section as part of the inlet (fig. 1), the curved surface into the alternate duct and the streamlines near the surface can be assumed to be concentric circular arcs. By starting at the surface point of tangency of the radius and nacelle-inlet section, the departure of droplets (based on Stokes' law) can be computed from reference 4 by

$$u = \frac{2}{9} \frac{c^2 v^2}{r_y \mu}$$

and

$$\delta = \int_{t_A}^{t_B} u \, dt$$

where

$u$  component of droplet local velocity normal to original streamline, ft/sec

$c$  droplet radius, ft

$v$  droplet velocity, ft/sec

$r_y$  streamline radius of curvature, ft

$\mu$  absolute air viscosity, lb-sec/sq ft

$\delta$  deviation of droplet normal to streamline, ft

$t$  time, sec

Subscripts A and B represent the limits of the time increment.

These equations only apply in the range of Stokes' law; a Reynolds number correction for velocity, however, has been made available by Langmuir (fig. 24). By choosing a true droplet diameter and referring to figure 24, the Stokes' law diameter can thus readily be determined and used in the previous equations.

By a graphical plot, the droplet flow paths can then be drawn and for a given design condition the location of the duct-splitter ring can be determined. The point of tangency between the droplet path and the outer surface of the duct-splitter ring should be located near a line passing through the center of the nacelle-wall radius and the surface-inflection point. Practical considerations, either aerodynamic or icing, may require slight revisions to this location.

For a simple analysis, the velocity in the duct is either considered constant or, if the velocity varies along a streamline, the average velocity can be used with sufficient accuracy. The analysis can be extended to calculate the secondary inertia separation in the elbow and other parts of the duct system.

The stub-nose or low critical Mach number nacelle designs, such as cowlings for reciprocating engines or jet-powered cargo planes, can also be analyzed. An inlet with a low inlet-velocity ratio or without a straight inlet section must be analyzed by assuming the streamlines ahead of the nacelle to be circular arcs. The analytical method presented herein is an approximation and should be used with caution.

The analytical method has been applied to a typical high inlet-velocity ratio full-scale nacelle of the type described in this report (fig. 1). If several initial droplet paths and streamlines are calculated from reference 4 for a desired flight condition, all the required droplet paths can be obtained by interpolation. The example shows that to prevent a maximum critical droplet size from entering an alternate inlet having a specified turning angle, the variation of inlet gap with inlet velocity is approximately a straight line (fig. 25). The maximum critical droplet size for the starting streamline, which is coincident with the nacelle surface or the configuration-design droplet size, was obtained; hence, the critical droplet sizes for starting streamlines inboard from the surface are then determined until the starting streamline no longer enters the alternate inlet (fig. 26). Droplets on those streamlines that miss the alternate-duct inlet are assumed to pass harmlessly into the main duct or impinge on the inner side of the duct-splitter ring. From the limiting streamline, a critical radius  $r_x$  is obtained below which, in accordance with the analysis assumptions, no droplet will enter the inlet. This critical radius is not attained in practice because streamlines crowd together in the alternate-duct inlet and are no longer circular arcs. At every  $r_x$  value between the nacelle-inlet radius  $r_1$  and the critical  $r_x$ , a critical droplet size exists and the percentage of these critical droplets that will enter the alternate-duct inlet to the number available at the nacelle inlet, or droplet-entry efficiency, can be obtained by the use of the following formula:

$$\left[ 1 - \left( \frac{r_x}{r_l} \right)^2 \right] 100$$

A typical example of the percentage of droplets that will enter an alternate-duct inlet shown in figure 27 was based on the following configuration characteristics;  $V_1 = 435$  miles per hour,  $\theta = 75^\circ$ ,  $r_l = 8.4$  inches,  $R = 4$  inches, and  $G = 2, 3$ , and 4 inches. The configuration design droplets of 22, 30, and 37 microns in figure 27 are shown to have a droplet-entry efficiency of 0, which indicates that droplets of this size have a nacelle-surface starting streamline and at the alternate-duct inlet are just tangent to the outer surface of the duct-splitter ring.

The water-volume variation with droplet size for a cloud sample and the volume percentages of the various droplet sizes that could enter the alternate-duct inlet are shown in figure 28. From the data and figure 28, it can be shown that 15.3 percent of the available water volume would enter the 3-inch gap inlet and 32.9 percent would enter the 4-inch gap inlet. Both inlet gaps thus considerably reduce the icing rate through the alternate duct.

## APPENDIX B

## ANALYSIS OF THE EFFECT OF RAM-PRESSURE RECOVERY ON ENGINE THRUST

The net thrust  $F$  of a turbojet engine is related to air flow rate  $w$ , speed of sound in jet  $v_j$ , jet Mach number  $M_j$ , and free-stream velocity  $V_0$  by the equation

$$F = \frac{w}{g} (v_j M_j - V_0) \quad (1)$$

The speed of sound in the jet is a function of the discharge temperature and is assumed to be constant for this analysis.

The jet Mach number is related to the total pressure of the jet  $P_3$  and free-stream static pressure  $p_0$  by the equation

$$M_j = \sqrt{\frac{2}{\gamma - 1} \left[ \left( \frac{P_3}{p_0} \right)^{\frac{\gamma - 1}{\gamma}} - 1 \right]} \quad (2)$$

The value of  $\gamma$  is approximately 1.36.

The pressure ratio  $P_3/p_0$  equals the product of the pressure ratio  $P_3/P_2$  across the engine, the pressure ratio  $P_2/p_0$  across the inlet, and the ram-pressure ratio  $P_0/p_0$ . Therefore,

$$\frac{P_3}{p_0} = \left( \frac{P_3}{P_2} \right) \left( \frac{P_2}{P_0} \right) \left( \frac{P_0}{p_0} \right)$$

$$\frac{P_3}{p_0} = \left( \frac{P_3}{P_2} \right) \left( \frac{P_2}{p_0} \right) \quad (3)$$

The pressure ratio across the engine is fixed by the engine characteristics and the engine operating speed.

The pressure ratio  $P_2/p_0$  is

$$\frac{P_2}{P_0} = 1 + \eta \left( \frac{P_0}{P_0} - 1 \right). \quad (4)$$

The value of  $P_3/P_0$  is found by substituting assumed values of  $\eta$  in equation (4) to find  $P_2/P_0$  and then substituting the resulting value of  $P_3/P_2$  in equation (3). The jet Mach number is then found from equation (2). The variation of weight flow with ram-pressure recovery can be expressed as

$$w = \frac{w'' \left[ 1 + \eta (P_0/P_0 - 1) \right]}{P_0/P_0} \quad (5)$$

where double prime indicates 100 percent ram-pressure recovery. This equation is based on the assumption that the corrected air flow at the compressor inlet is uniform and constant.

The net thrust ratio can now be written as

$$F/F_{\max} = \frac{w/g (v_j M_j - v_0)}{w''/g (v_j'' M_j'' - v_0)} \quad (6)$$

or

$$F/F_{\max} = \frac{\left[ 1 + \eta (P_0/P_0 - 1) \right] (v_j - v_0)}{P_0/P_0 (v_j'' - v_0)} \quad (7)$$

For the example presented, the performance of the engine was calculated for a pressure altitude of 20,000 feet and free-stream Mach numbers of 0.2, 0.4, and 0.6. Three engine pressure ratios of  $P_3/P_2$  of 1.6, 2.0, and 2.4 were assumed and covered the usual engine operation range. A constant velocity of sound in the jet of 1600 feet per second was assumed to satisfy equation (2). The results of the calculations are presented in figure 15.

#### REFERENCES

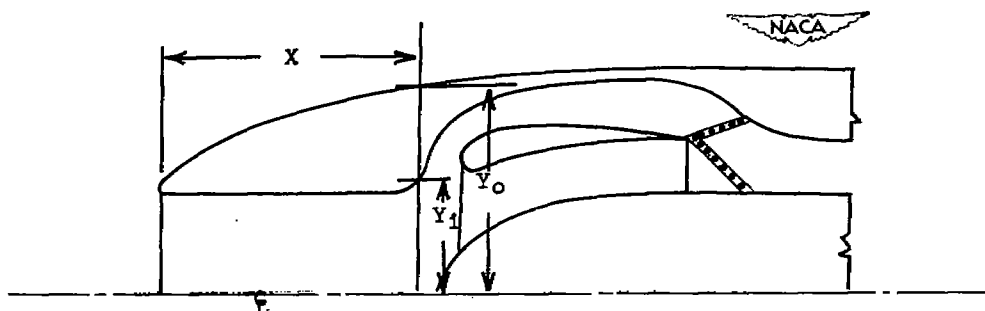
1. von Glahn, Uwe, and Renner, Clark E.: Development of a Protected Air Scoop for the Reduction of Induction-System Icing. NACA TN No. 1134, 1946.

2. Baals, Donald D., Smith, Norman F., and Wright, John B.: The Development and Application of High-Critical-Speed Nose Inlets NACA ACR No. L5F30a, 1945.
3. Cohen, Herbert N.: Investigation of Intake Ducts for a High-Speed Subsonic Jet-Propelled Airplane. NACA RM No. L7C24a, 1947.
4. Stickley, A. R.: Some Remarks on the Physical Aspects of the Aircraft Icing Problem. Jour. Aero. Sci., vol. 5, no. 11, Sept. 1938, pp. 442-446.



TABLE I - NACELLE- AND SPINNER-CONTOUR COORDINATES WITH  
REFERENCE TO THE NACELLE LEADING EDGE AND CENTER LINE

[1, inside contour and o; outside contour;  
all values in inches]



Outside nacelle-surface coordinates; leading-edge radius, 0.15							
X	Y <sub>o</sub>	X	Y <sub>o</sub>	X	Y <sub>o</sub>	X	Y <sub>o</sub>
0	4.35	1.58	5.70	8.19	7.91	17.01	9.45
.06	4.50	2.52	6.16	9.45	8.19	18.90	9.68
.19	4.70	3.46	6.55	10.71	8.45	22.05	9.97
.25	4.77	4.72	6.98	11.97	8.68	25.20	10.18
.63	5.11	5.67	7.27	13.23	8.90	27.09	10.27
1.10	5.43	6.93	7.60	15.12	9.19	31.50	10.35

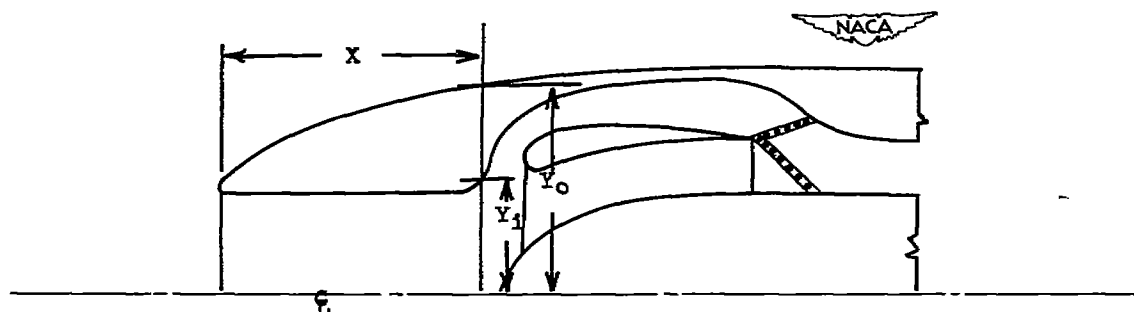
Nose N-1 and inside nacelle-wall coordinates for configurations A-1, A-2, A-3, A-6, and A-7									
X	Y <sub>i</sub>	X	Y <sub>i</sub>	X	Y <sub>i</sub>	X	Y <sub>i</sub>	X	Y <sub>i</sub>
1.00	4.20	11.00	4.31	14.00	7.96	16.50	8.88	27.00	9.50
4.00	4.20	12.00	4.47	14.50	8.31	17.06	8.97	29.13	9.12
8.00	4.20	12.50	5.19	15.00	8.56	18.94	9.16	30.38	8.38
10.00	4.20	13.00	5.94	15.50	8.69	22.06	9.38	34.63	7.25
10.50	4.22	13.50	7.25	16.00	8.78	25.19	9.50	37.63	7.25

Modified inside nacelle-wall coordinates; for configurations A-4 and A-5									
X	Y <sub>i</sub>	X	Y <sub>i</sub>	X	Y <sub>i</sub>	X	Y <sub>i</sub>	X	Y <sub>i</sub>
10.00	4.20	14.00	7.25	15.50	8.38	17.00	8.87	18.94	9.16
13.00	5.87	14.50	7.72	16.00	8.59	17.50	8.97	22.06	9.38
13.50	6.59	15.00	8.09	16.50	8.75	18.00	9.06	25.19	9.50

Accessory-housing nose coordinates; nose radius, 3.00									
X		Y		X		Y			
17.50		0		20.50		3.88		23.50	
19.00		2.81		22.00		4.44		26.12	
								4.75	
								5.00	

TABLE II - COORDINATES FOR NACELLE-NOSE SECTIONS N-2,  
N-3, AND N-4 WITH REFERENCE TO THE LEADING EDGE OF  
NOSE N-1 AND NACELLE CENTER LINE

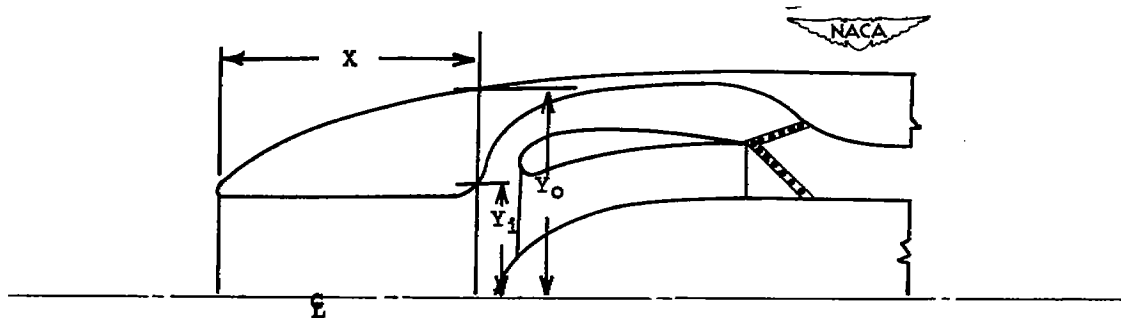
[i, inside contour and o, outside contour; all  
values in inches]



X	$Y_i$	X	$Y_i$
Nacelle nose N-2; leading- edge radius, 0.31			
0.12	4.75	1.12	4.28
.62	4.37	1.87	4.20
Nacelle nose N-3; leading- edge radius, 0.37			
0.80	5.20	2.75	4.50
1.50	4.70	10.50	4.20
Nacelle nose N-4; leading- edge radius, 0.37			
0.95	5.20	1.75	4.80
1.30	4.85	10.62	4.65
11.50	4.85	13.00	6.15
12.50	5.50	13.50	7.30

TABLE III - COORDINATES FOR DUCT-SPLITTER RINGS REFERENCED  
FROM NACELLE NOSE N-1 LEADING EDGE AND NACELLE CENTER LINE

[i, inside contour and o, outside contour;  
all values in inches]



X	Y <sub>i</sub>	Y <sub>o</sub>	X	Y <sub>i</sub>	Y <sub>o</sub>	X	Y <sub>i</sub>	Y <sub>o</sub>
Configuration A-1; leading-edge radius, 0.625								
13.81	5.75	5.75	16.31	5.94	8.22	20.31	7.22	8.10
14.31	6.06	7.12	16.81	6.22	8.28	21.31	7.37	-
14.81	6.09	7.59	17.31	6.44	8.28	22.31	7.50	-
15.31	5.31	7.93	18.31	6.81	8.26	29.06	7.50	7.69
15.81	5.62	8.15	19.31	7.03	8.15			
Configuration A-2; leading-edge radius, 0.500								
14.87	6.40	6.40	17.37	6.12	7.31	19.87	7.18	7.63
15.37	4.87	6.25	17.87	6.44	7.47	20.37	7.25	7.63
15.87	4.97	6.66	18.37	6.66	7.57	20.87	7.38	7.63
16.37	5.19	6.94	18.87	6.88	7.63	21.37	7.44	7.63
16.87	5.66	7.13	19.37	7.03	7.63	22.37	7.50	7.63
Configuration A-3; leading-edge radius, 0.188								
15.90	6.28	6.28	17.90	6.75	7.47	19.90	7.19	7.63
16.40	6.22	6.94	18.40	6.91	7.57	20.40	7.25	7.63
16.90	6.44	7.19	18.90	7.03	7.62	20.90	7.31	7.63
17.40	6.59	7.34	19.40	7.12	7.63	22.90	7.50	7.63
Configuration A-4; leading-edge radius, 0.500								
13.87	5.38	5.38	16.37	5.97	7.35	18.87	6.94	7.63
14.37	4.88	6.26	16.87	6.25	7.47	19.37	7.06	7.63
14.87	4.97	6.66	17.37	6.47	7.56	20.37	7.25	7.63
15.37	5.19	6.94	17.87	6.66	7.63	21.37	7.41	7.63
15.87	5.62	7.15	18.37	6.81	7.63	22.37	7.50	7.63
Configuration A-5; leading-edge radius, 0.188								
14.75	6.40	6.40	17.25	6.78	7.53	19.75	7.19	7.63
15.25	6.22	6.94	17.75	6.88	7.60	20.25	7.25	7.63
15.75	6.38	7.19	18.25	6.97	7.63	20.75	7.31	7.63
16.25	6.53	7.34	18.75	7.06	7.63	21.25	7.38	7.63
16.75	6.66	7.47	19.25	7.12	7.63	22.25	7.50	7.63
Configuration A-6; leading-edge radius, 0.625								
14.18	5.75	5.75	16.68	5.94	8.22	20.31	7.22	8.10
14.68	5.06	7.12	17.18	6.22	8.28	21.68	7.37	-
15.18	5.09	7.59	17.68	6.44	8.28	22.68	7.50	-
15.68	5.31	7.93	18.68	6.81	8.26	29.06	7.50	7.69
16.18	5.62	8.15	19.68	7.03	8.15			
Configuration A-7; leading-edge radius, 0.500								
14.38	5.78	5.78	16.38	6.12	7.75	19.38	7.12	8.25
14.88	5.28	7.12	16.88	6.36	7.91	20.38	7.31	-
15.38	5.50	7.48	17.38	6.62	7.99	21.38	7.50	-
15.88	5.81	7.62	18.38	6.94	8.19	25.94	7.50	7.69

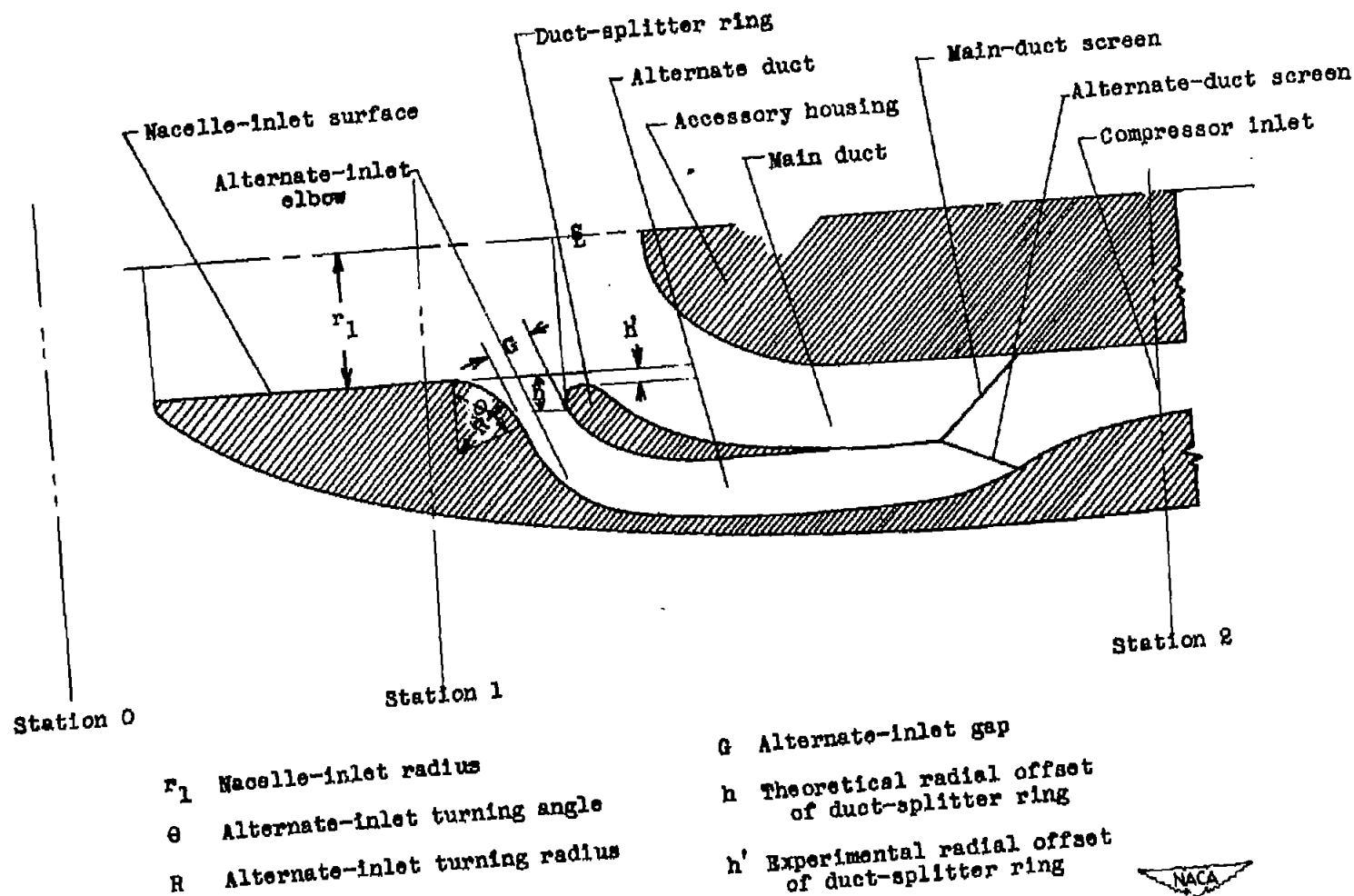
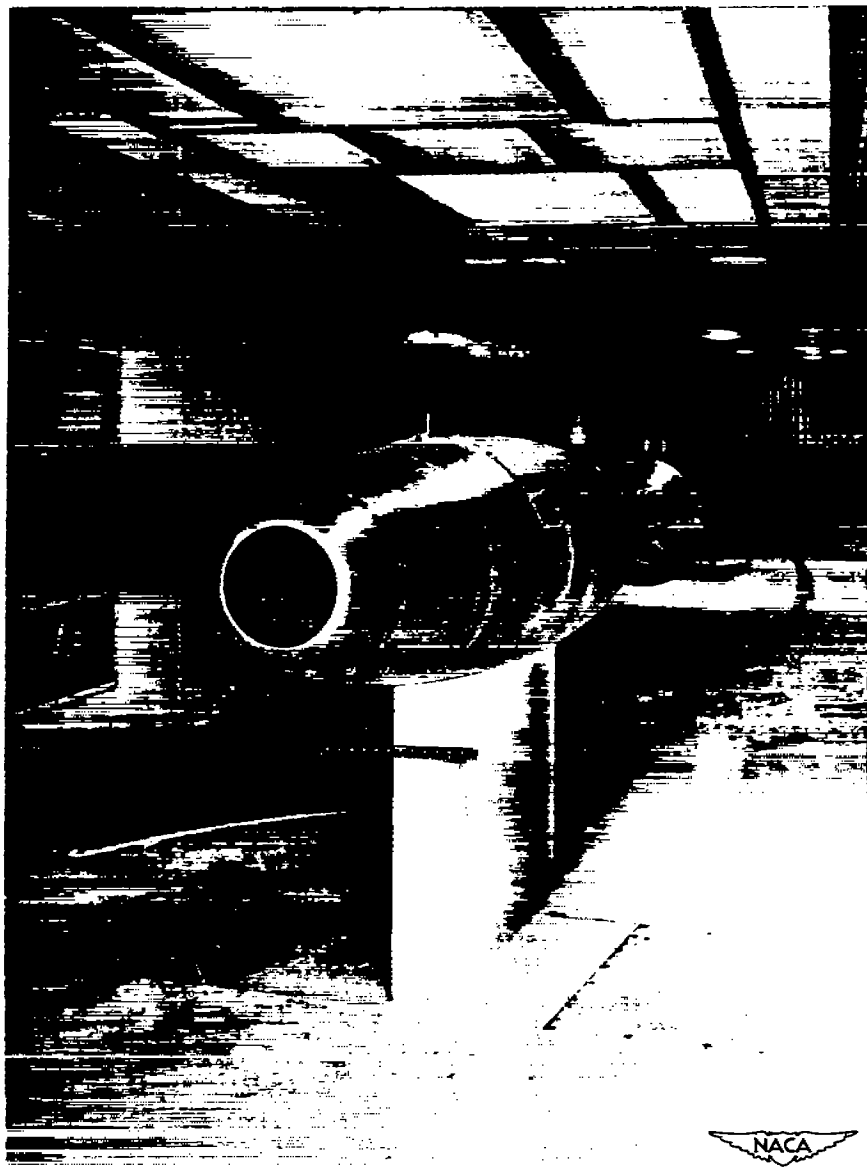


Figure 1.- Typical high-critical Mach number internal water-inertia separation inlet showing principal components.

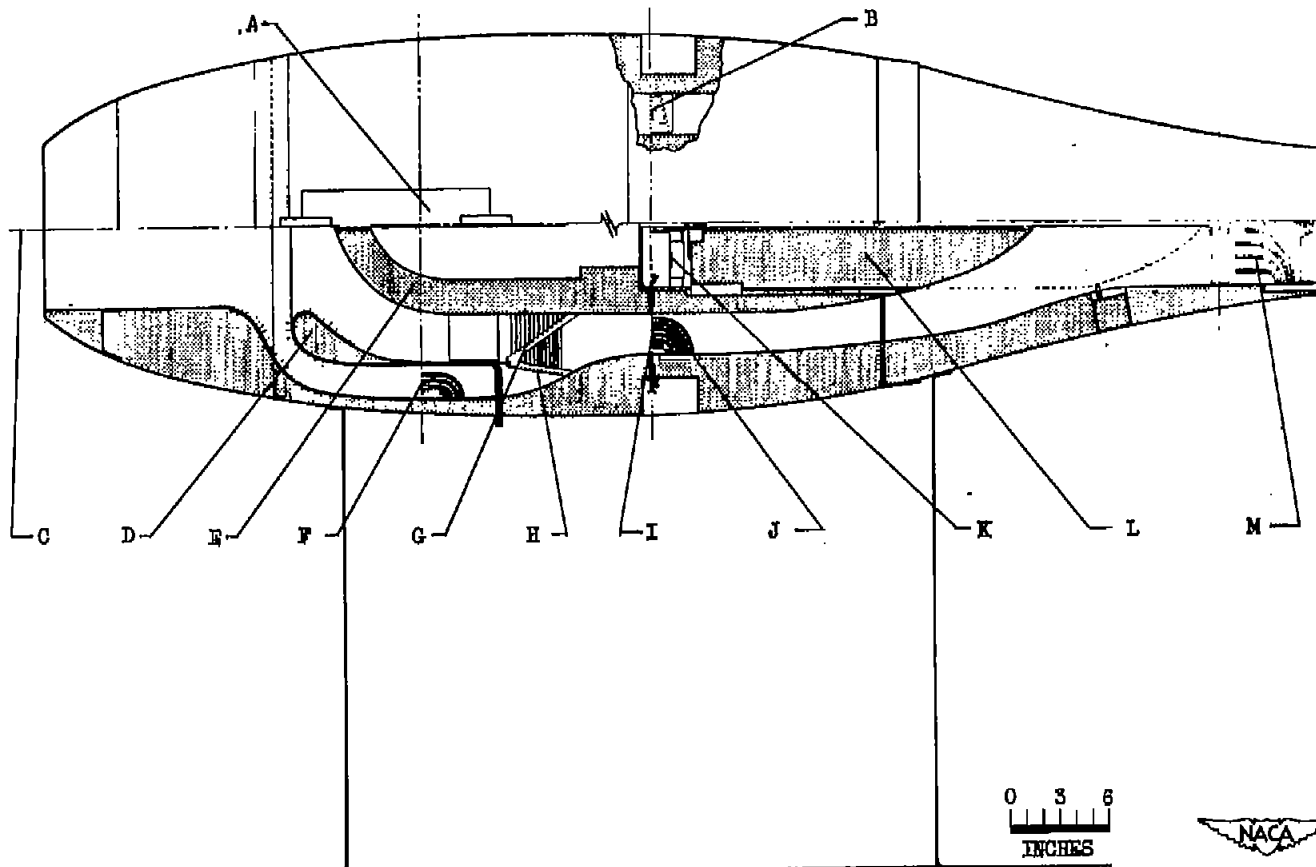




C-18727  
5-13-47

Figure 2. - Installation of typical internal water-inertia separation nacelle inlet in icing research tunnel.





A Alternate-duct inspection door  
 B Unheated total-pressure rakes  
 C Nacelle and tunnel center line  
 D Duct-splitter ring  
 E Accessory housing

F Alternate-duct instrumentation plane  
 G Main-duct screen  
 H Alternate-duct screen  
 I Compressor-inlet instrumentation plane

J Heated total-pressure rakes  
 K Tail-cone drive  
 L Tail cone  
 M Heated total-pressure rakes

Figure 3. - Schematic diagram of internal water-inertia separation nacelle-inlet installation.



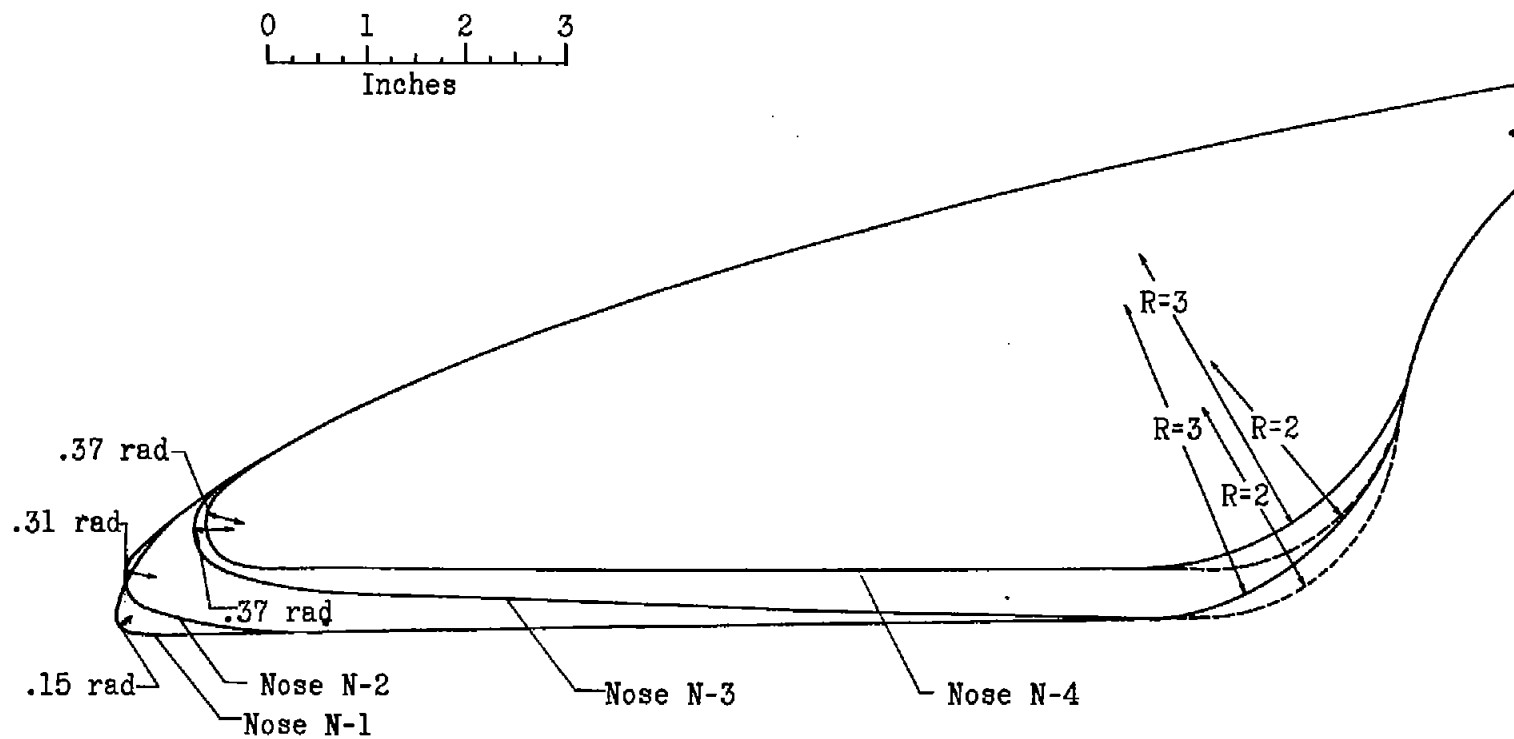
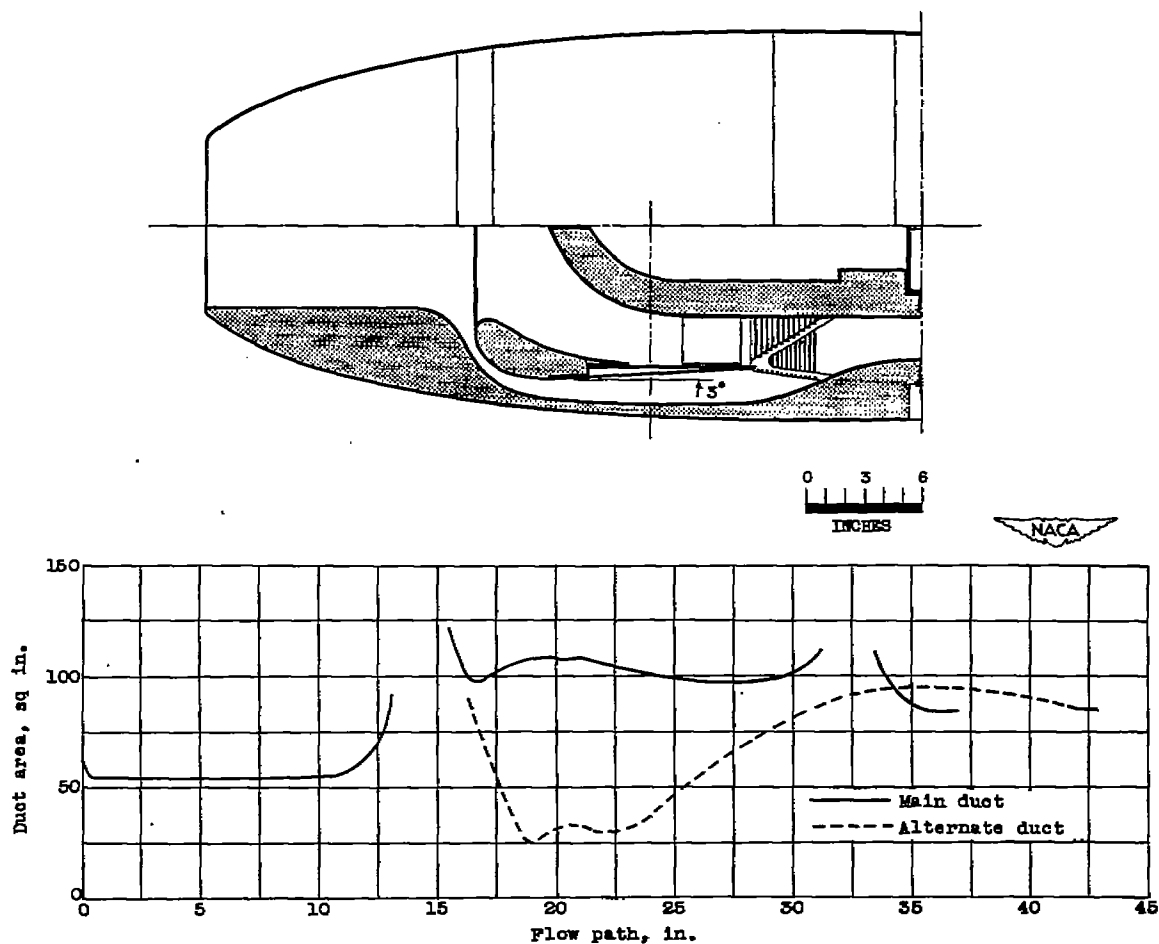


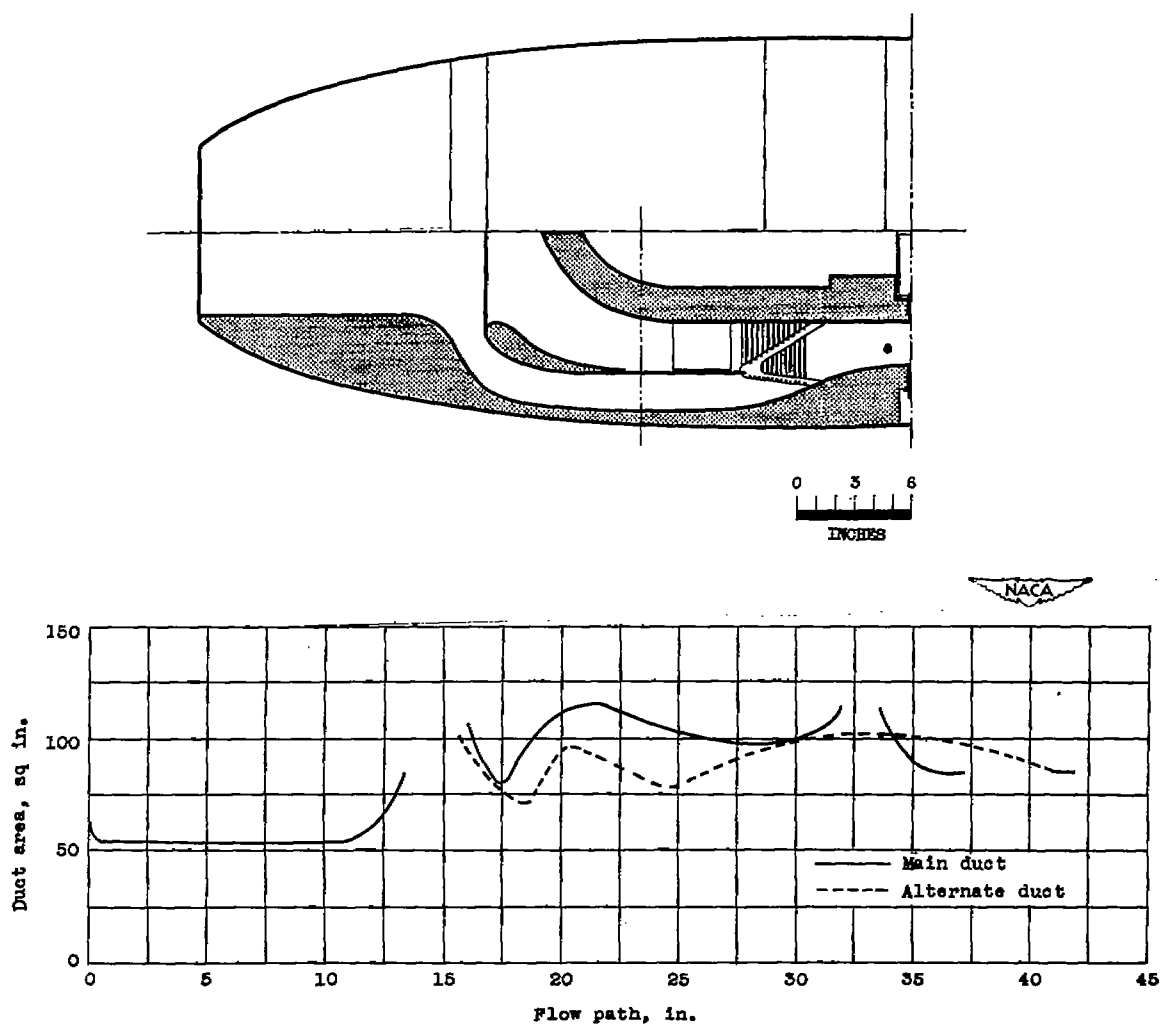
Figure 4.- Nacelle-nose contours.





(a) Configuration A-1.

Figure 5.- Cross sections and area graphs for internal water-inertia separation inlets with nose N-1.

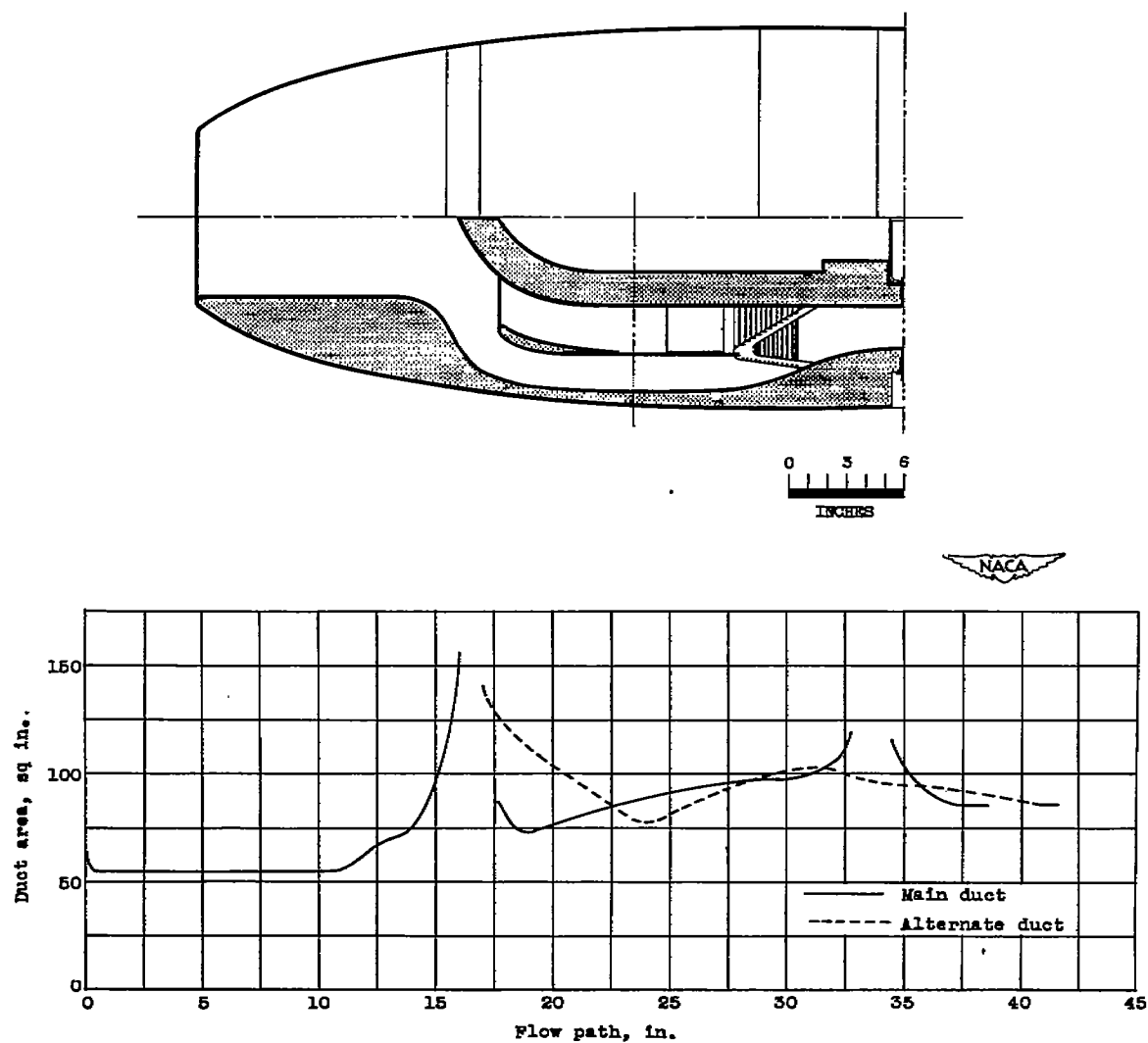


(b) Configuration A-2.

Figure 5.- Continued. Cross sections and area graphs for internal water-inertia separation inlets with nose W-1.

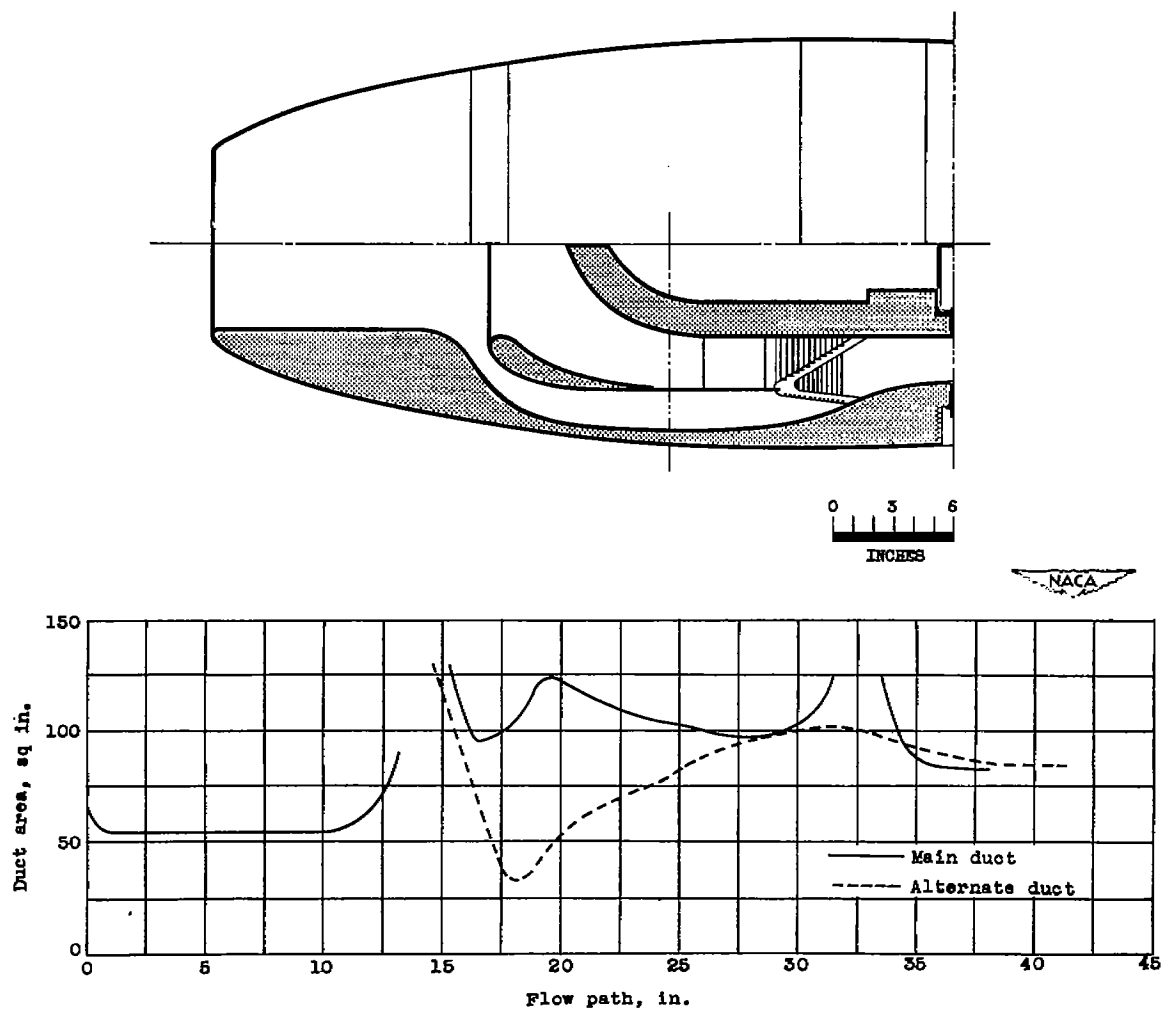
900

306-1022



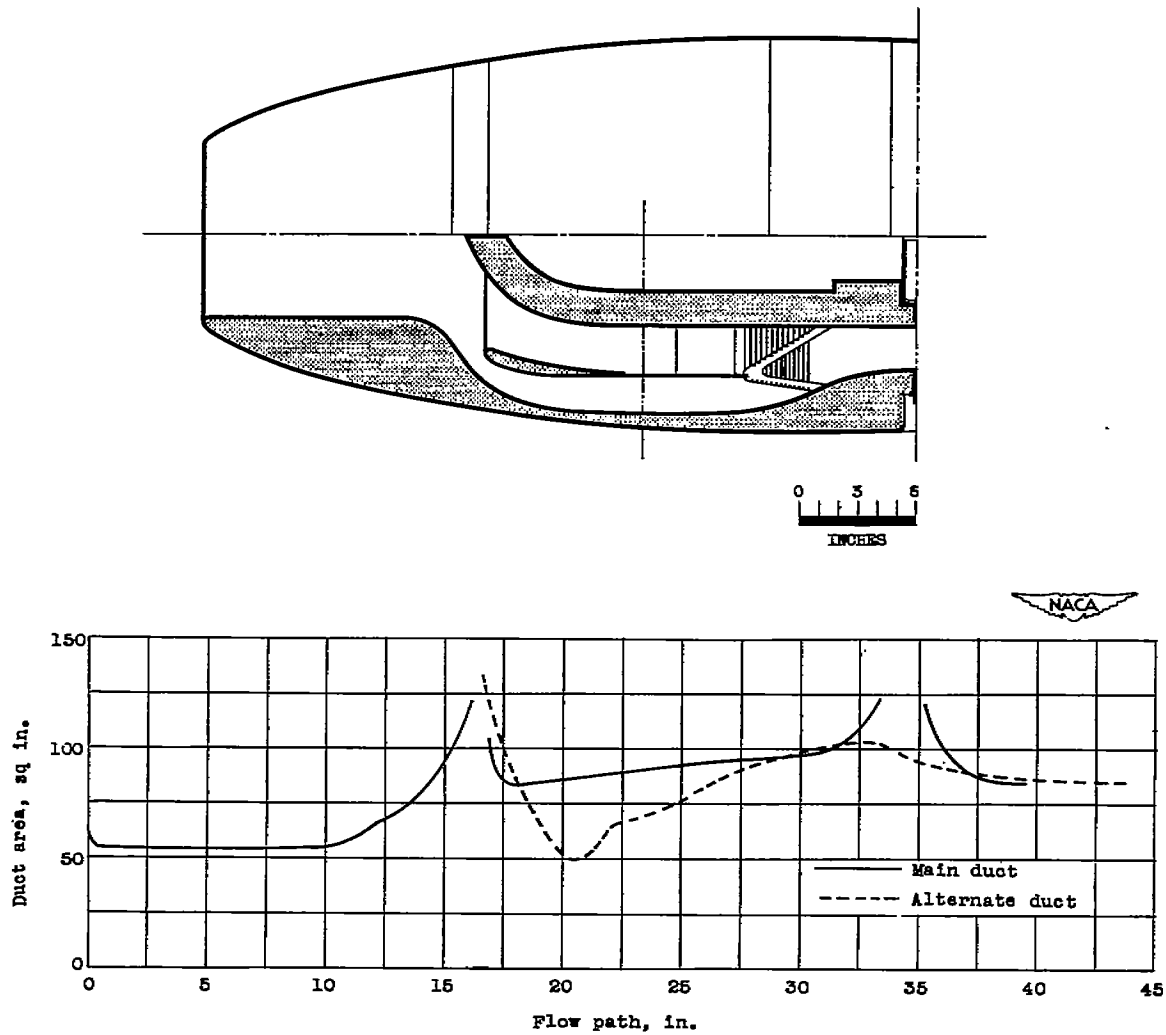
(c) Configuration A-3.

Figure 5.- Continued. Cross sections and area graphs for internal water-inertia separation inlets with nose N-1.



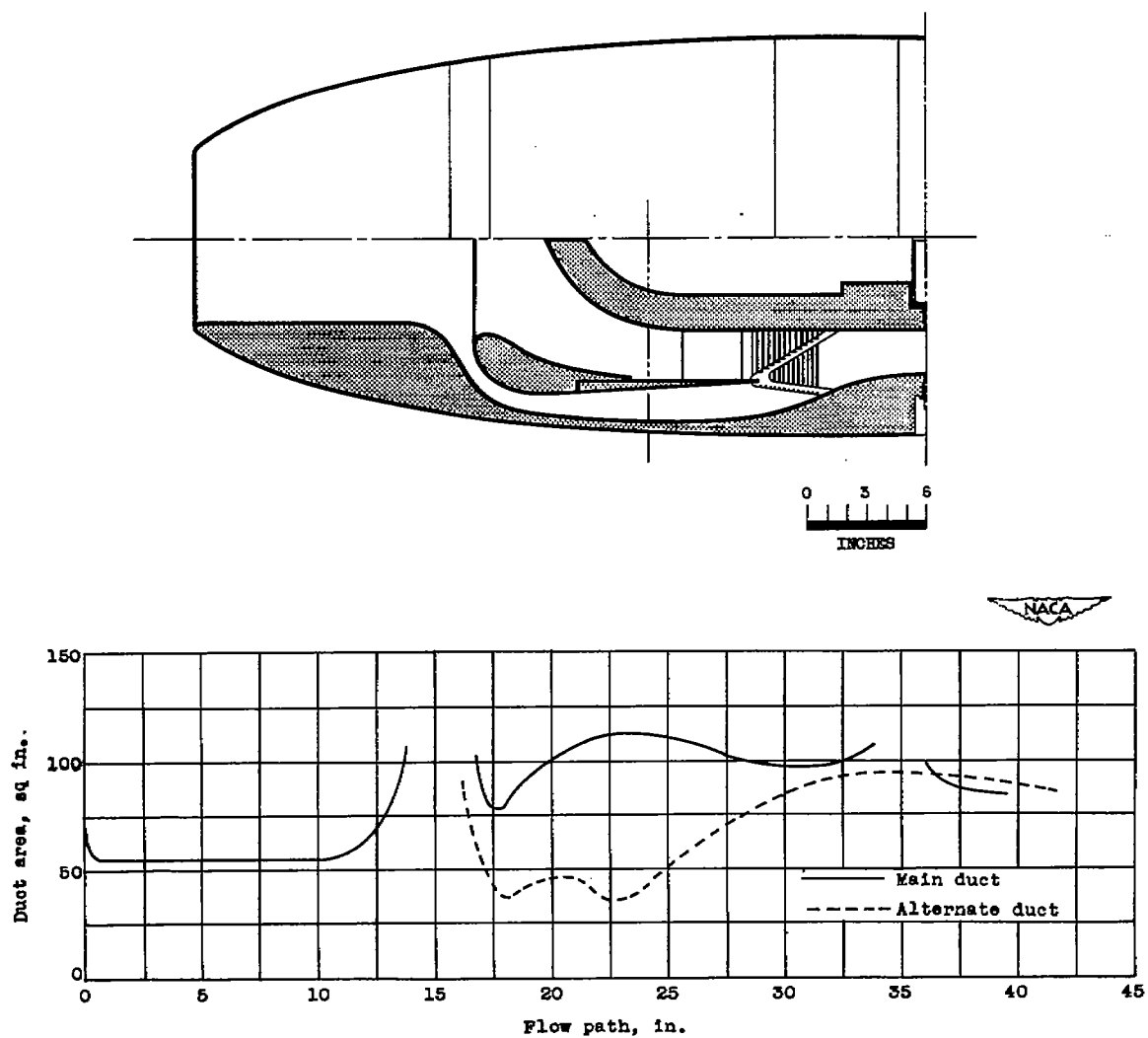
(d) Configuration A-4.

Figure 5.- Continued. Cross sections and area graphs for internal water-inertia separation inlets with nose N-1.



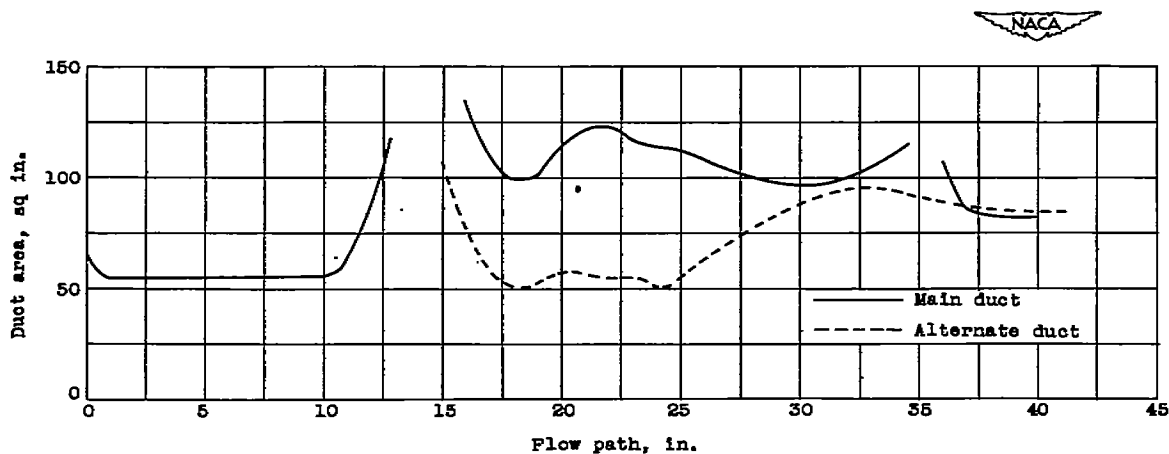
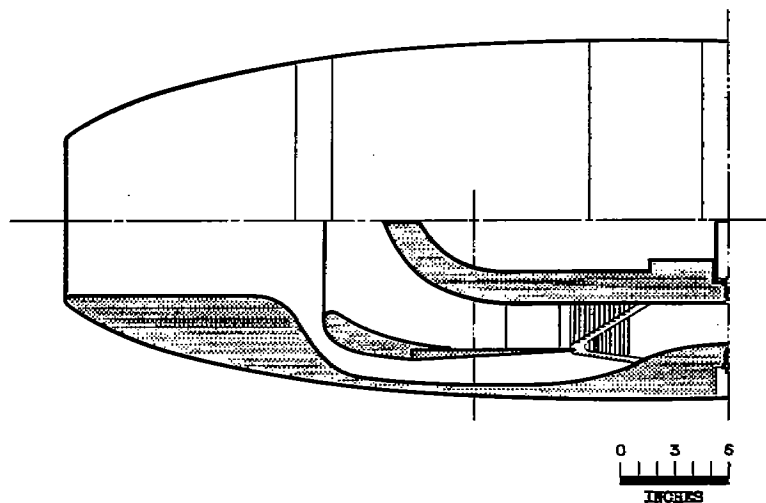
(e) Configuration A-5.

Figure 5.- Continued. Cross sections and area graphs for internal water-inertia separation inlets with nose N-1.



(f) Configuration A-6.

Figure 5.- Continued. Cross sections and area graphs for internal water-inertia separation inlets with nose N-1.



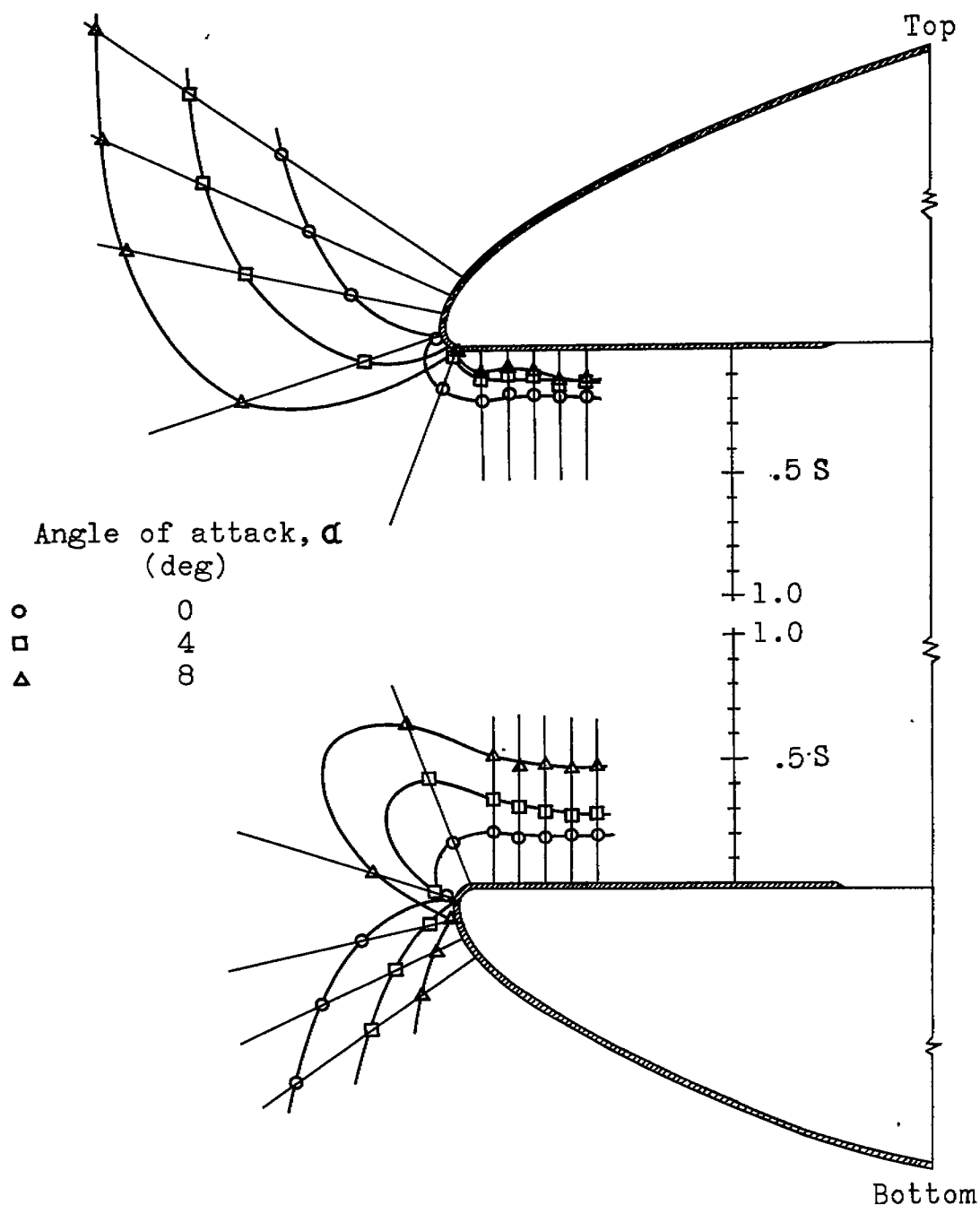
(g) Configuration A-7.

Figure 5.- Concluded. Cross sections and area graphs for internal water-inertia separation inlets with nose N-1.

900

306-1093



(a) Nose N-1;  $V_1/V_0$ , 0.45.Figure 6.- Surface pressure distribution about nacelle-inlet nose. Free-stream Mach number  $M_0$ , 0.4.

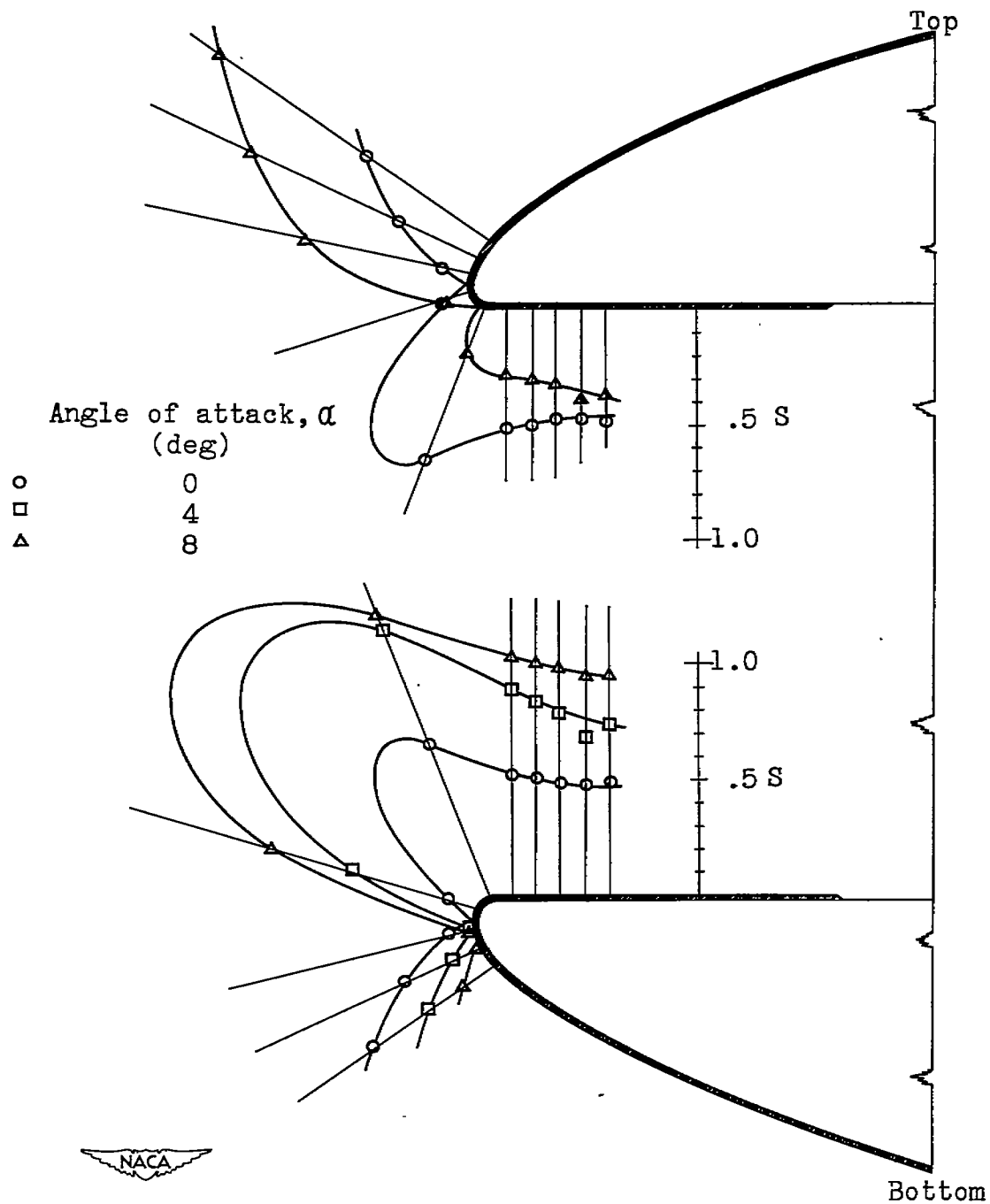
(b) Nose N-1;  $V_1/V_0$ , 0.70.

Figure 6.- Continued. Surface pressure distribution about nacelle-inlet nose. Free-stream Mach number  $M_0$ , 0.4.

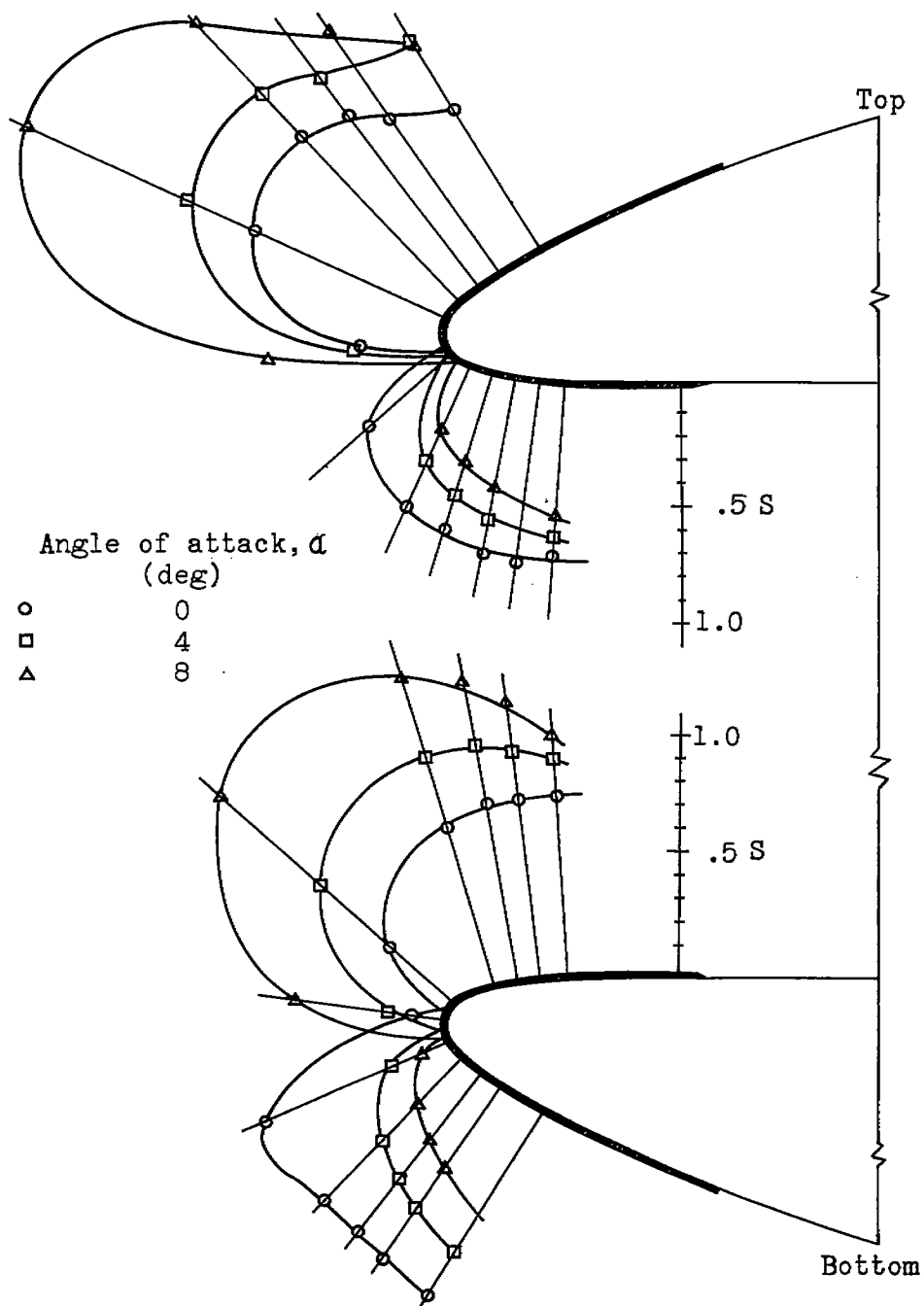
(c) Nose N-2;  $V_1/V_0$ , 0.82.

Figure 6.- Continued. Surface pressure distribution about nacelle-inlet nose. Free-stream Mach number  $M_0$ , 0.4.

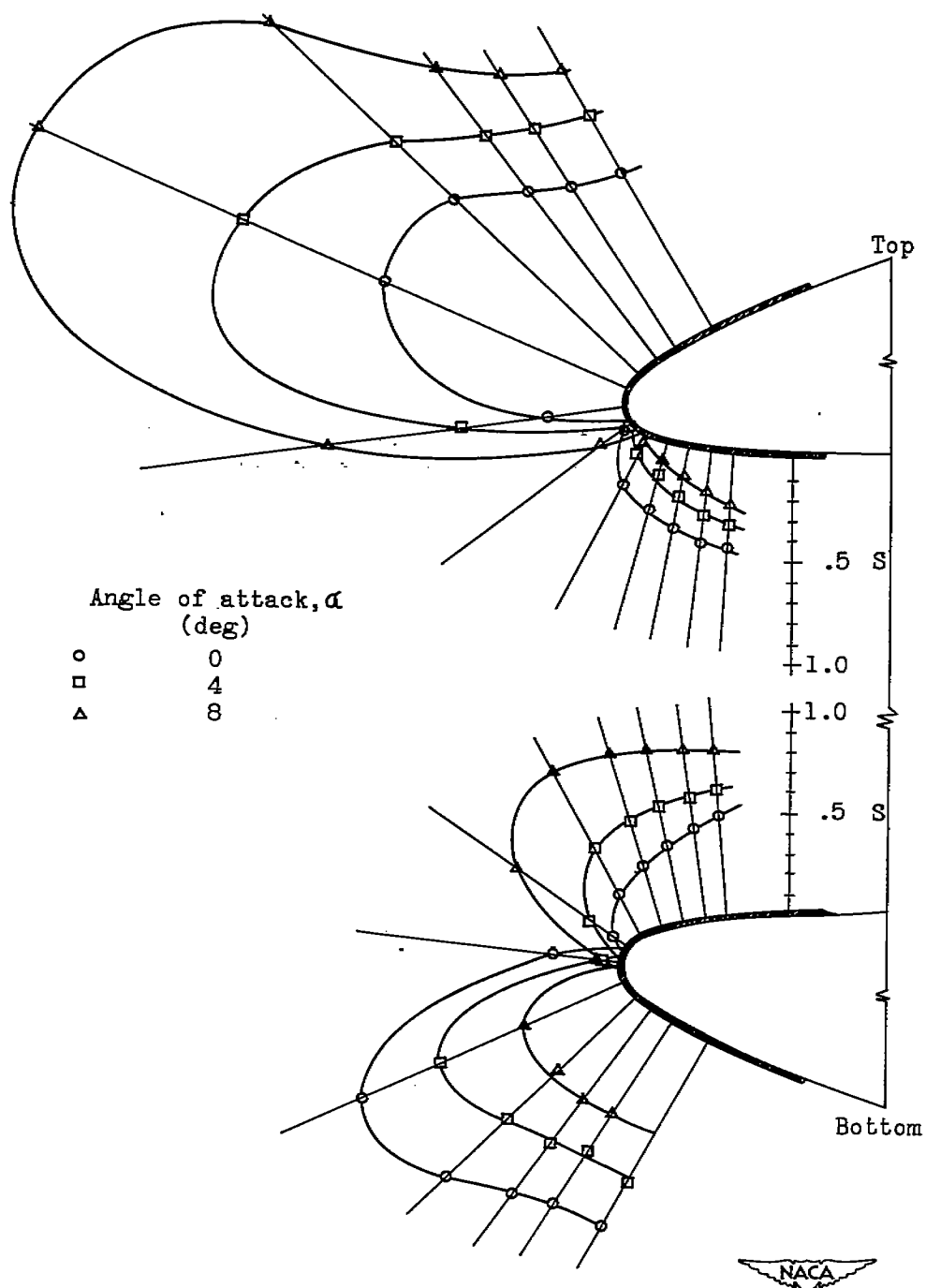
(d) Nose N-3;  $V_1/V_0$ , 0.80.

Figure 6.- Continued. Surface pressure distribution about nacelle-inlet nose. Free-stream Mach number  $M_0$ , 0.4.

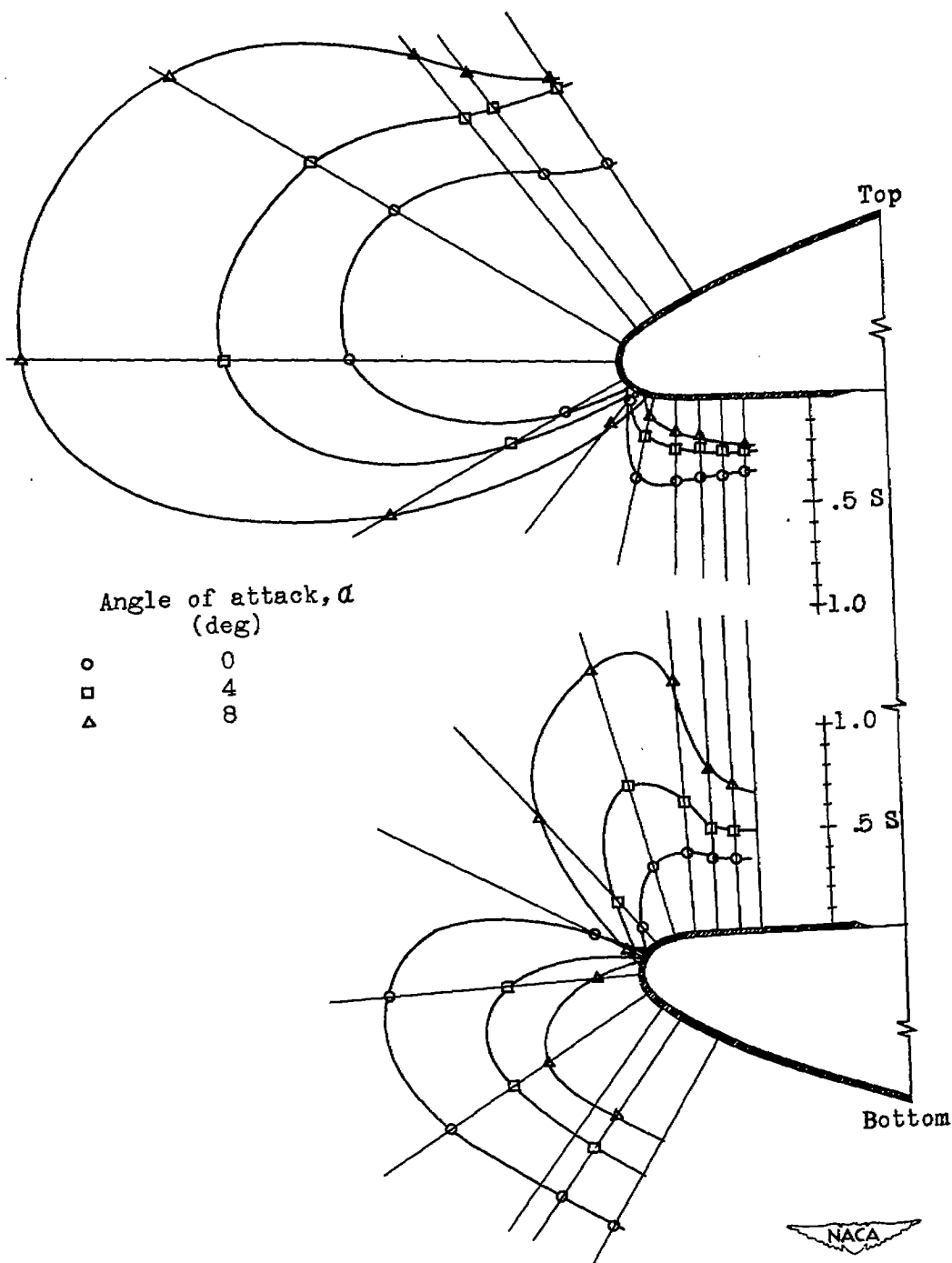
(e) Nose N-4;  $V_1/V_0$ , 0.67.

Figure 6.- Concluded. Surface pressure distribution about nacelle-inlet nose. Free-stream Mach number  $M_0$ , 0.4.

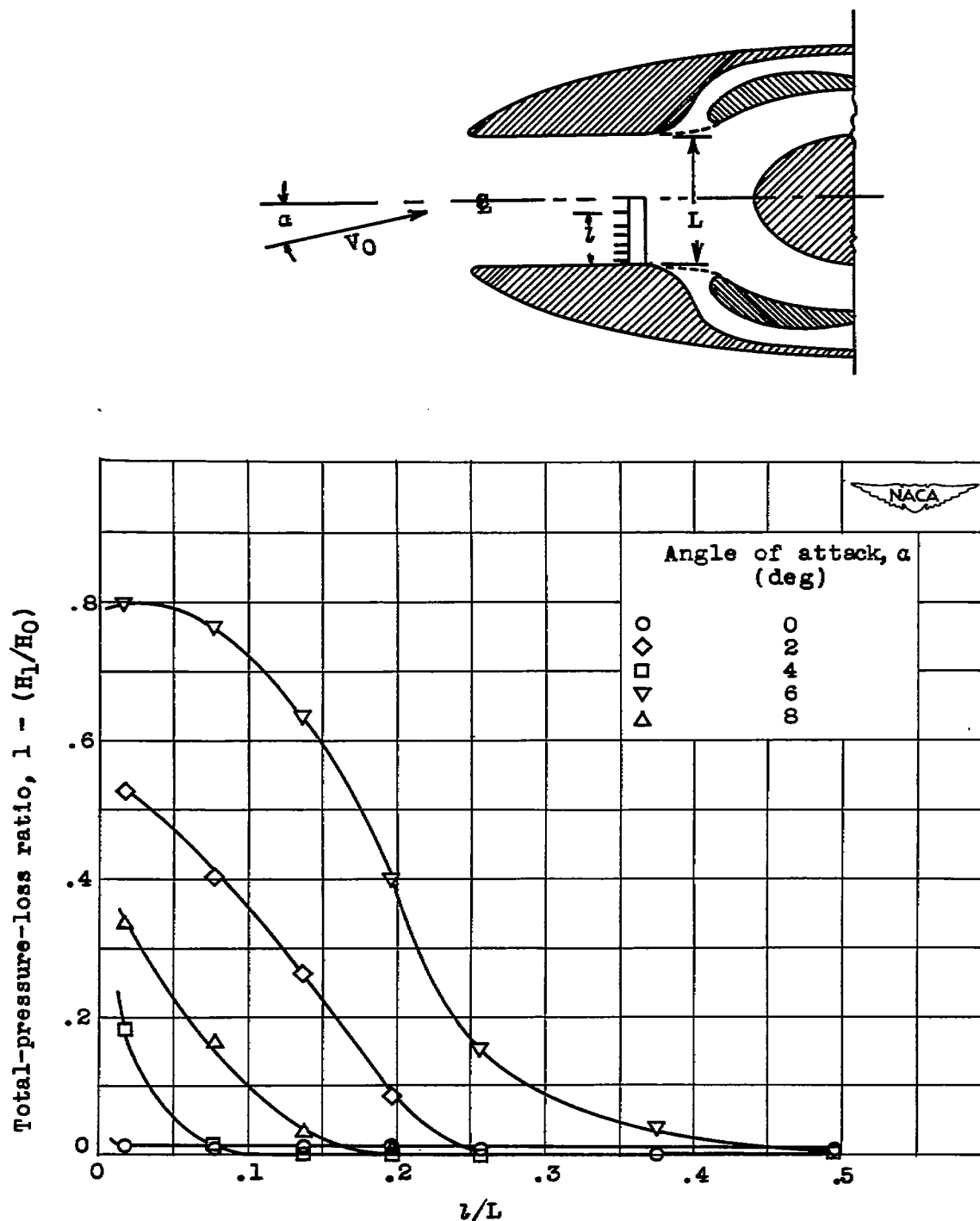
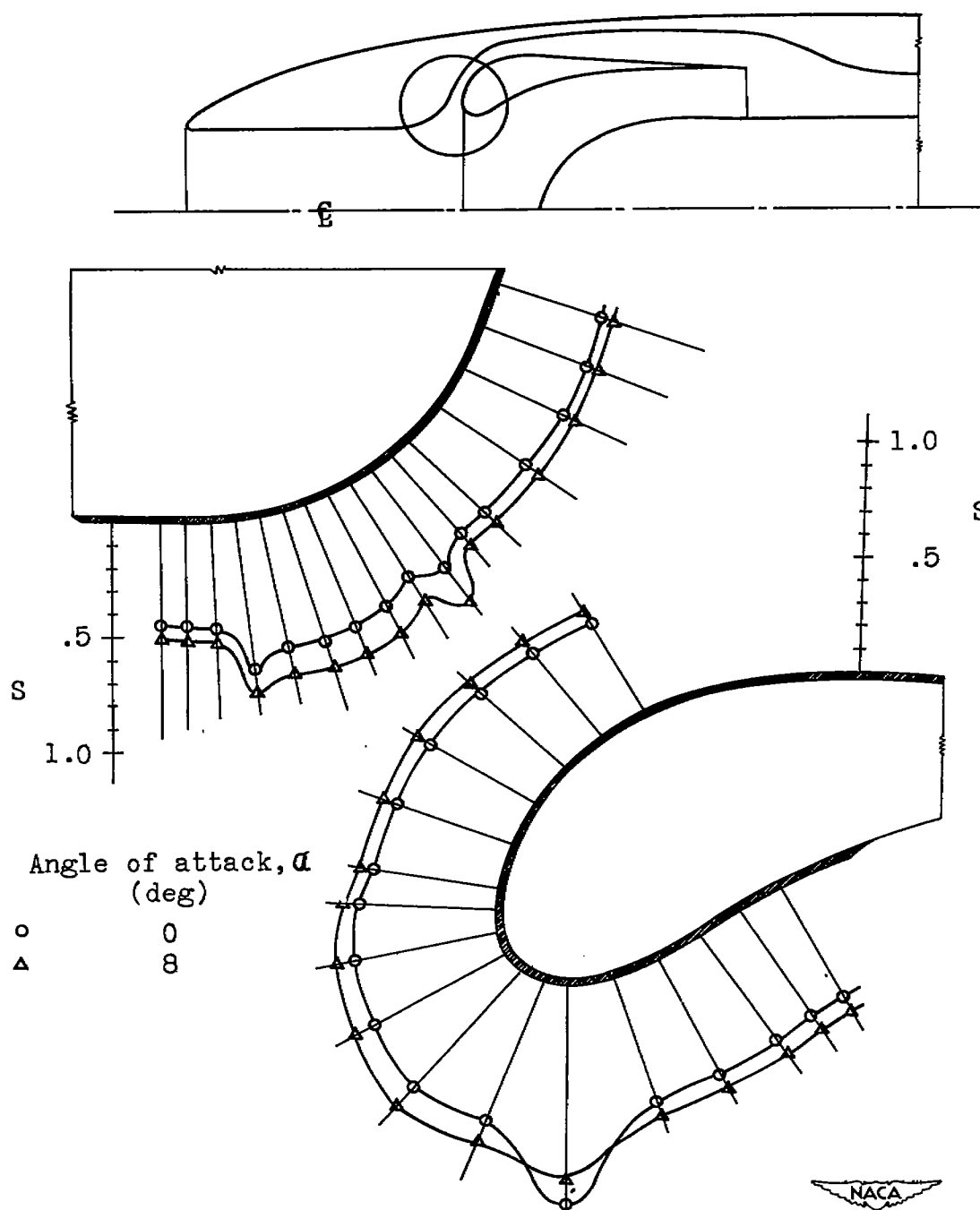


Figure 7.- Effect of angle of attack on total-pressure losses across bottom of inlet section on direct-ram configuration. Airspeed  $V_0$ , 280 miles per hour; inlet-velocity ratio  $V_1/V_0$ , 0.83.



(a) Configuration A-1.

Figure 8.- Surface pressure distribution at alternate-duct inlet of nose N-1. Normal operation; inlet-velocity ratio  $V_1/V_0$ , 0.70.

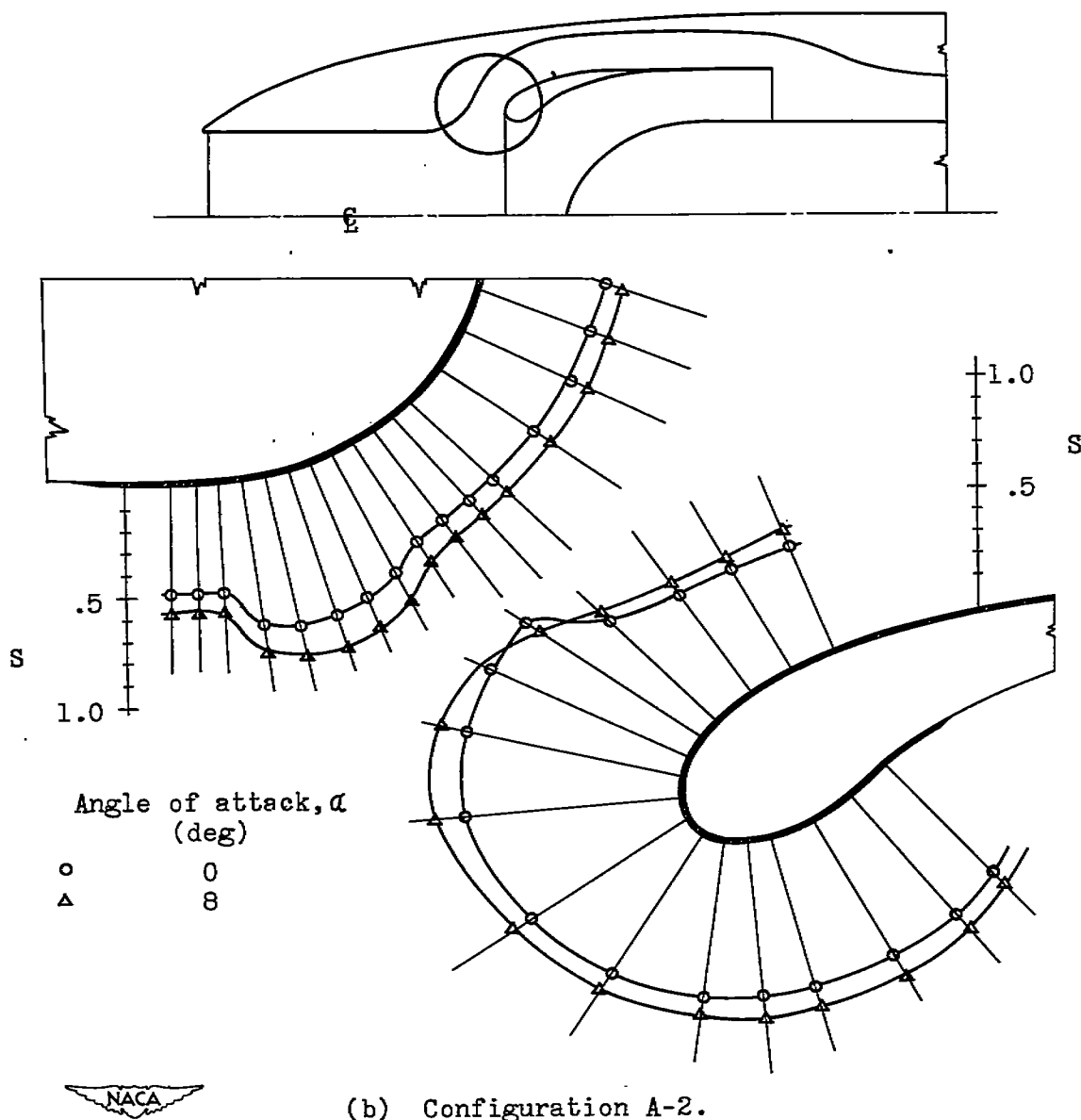


Figure 8.- Continued. Surface pressure distribution at alternate-duct inlet of nose N-1. Normal operation; inlet-velocity ratio  $V_1/V_0$ , 0.70.



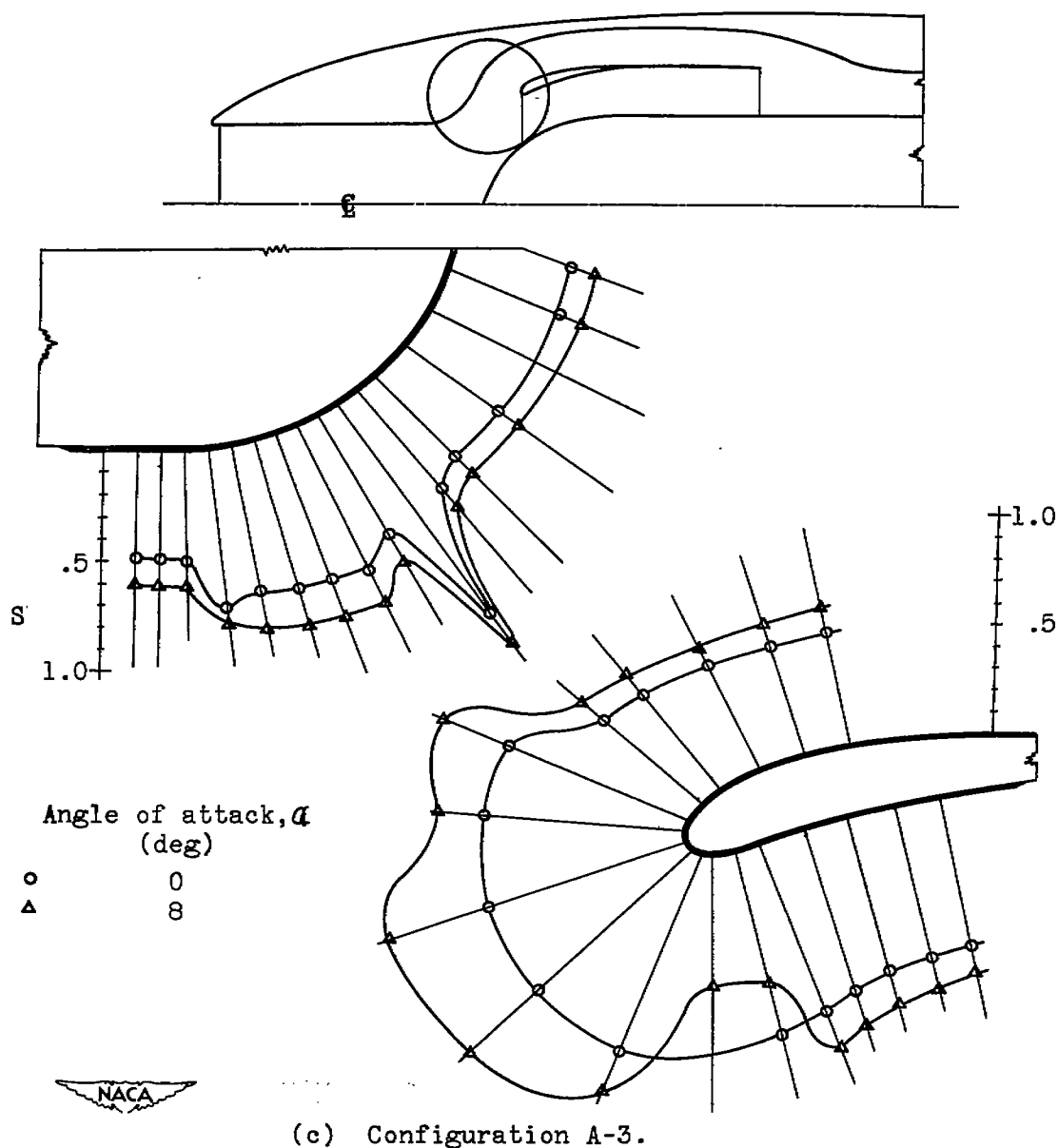
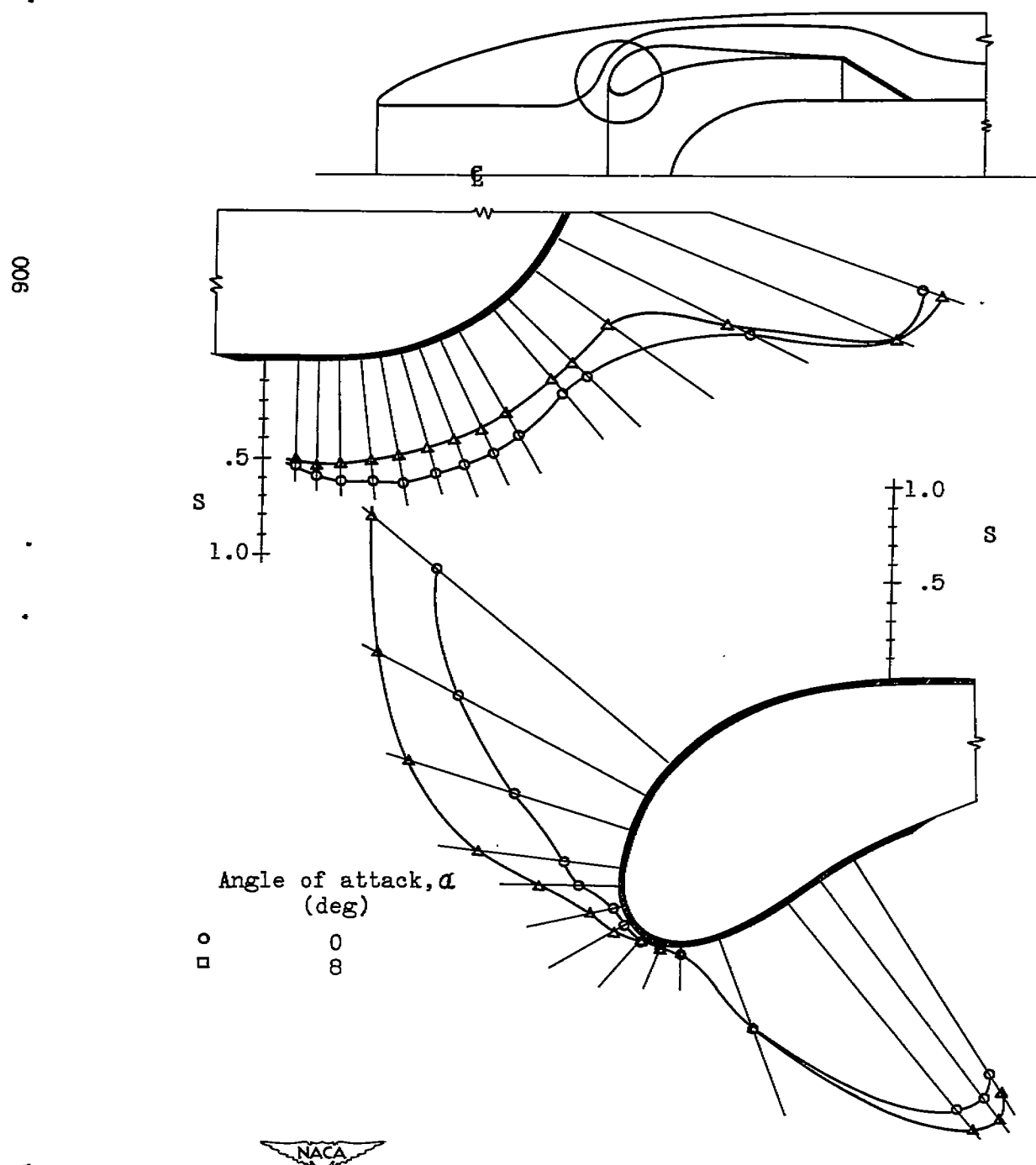


Figure 8.- Concluded. Surface pressure distribution at alternate-duct inlet of nose N-1. Normal operation; inlet-velocity ratio  $V_1/V_0$ , 0.70.



(a) Configuration A-1.

Figure 9.- Surface pressure distribution at alternate-duct inlet of nose N-1. Main duct blocked; inlet-velocity ratio  $V_1/V_0$ , 0.70.

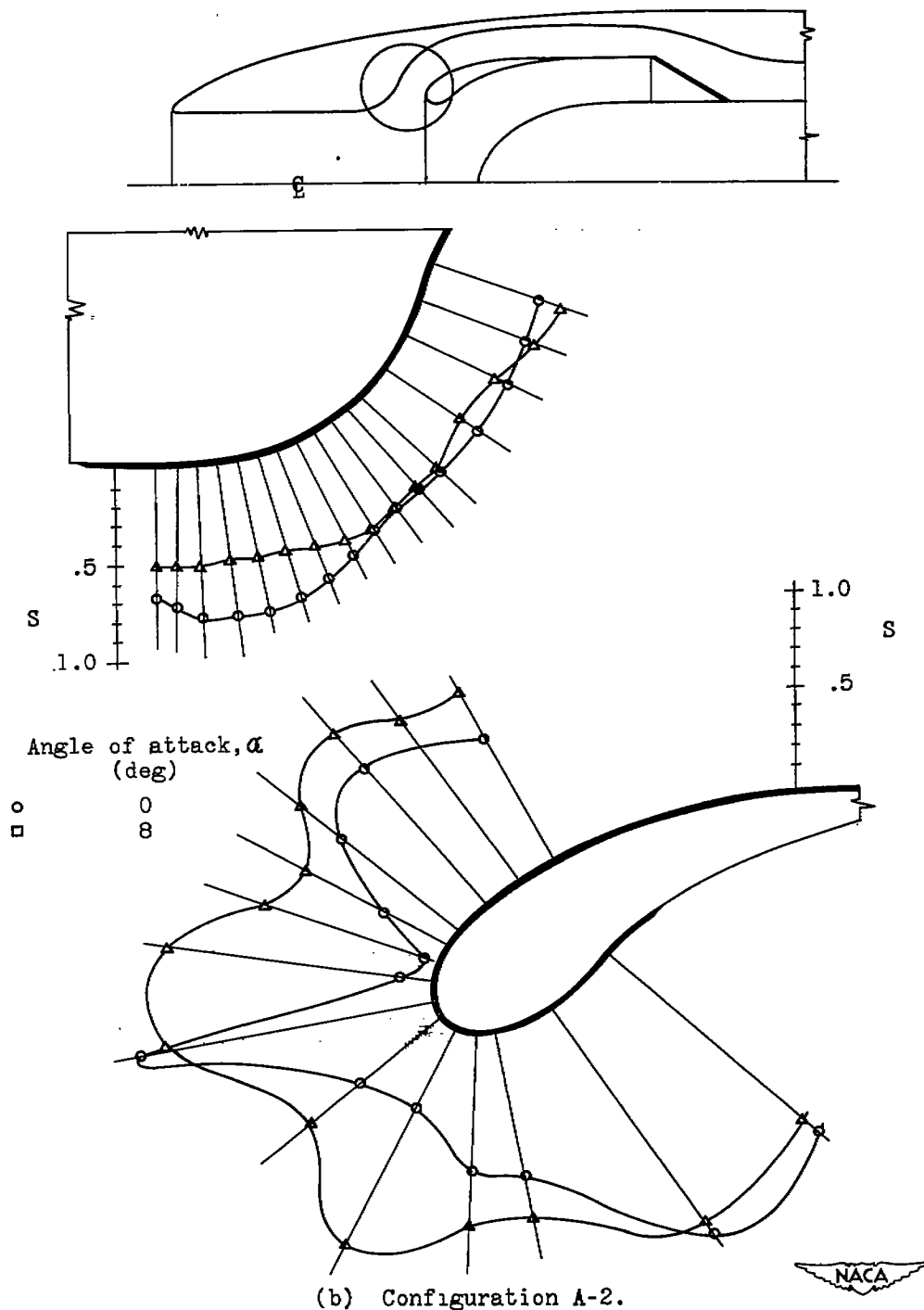
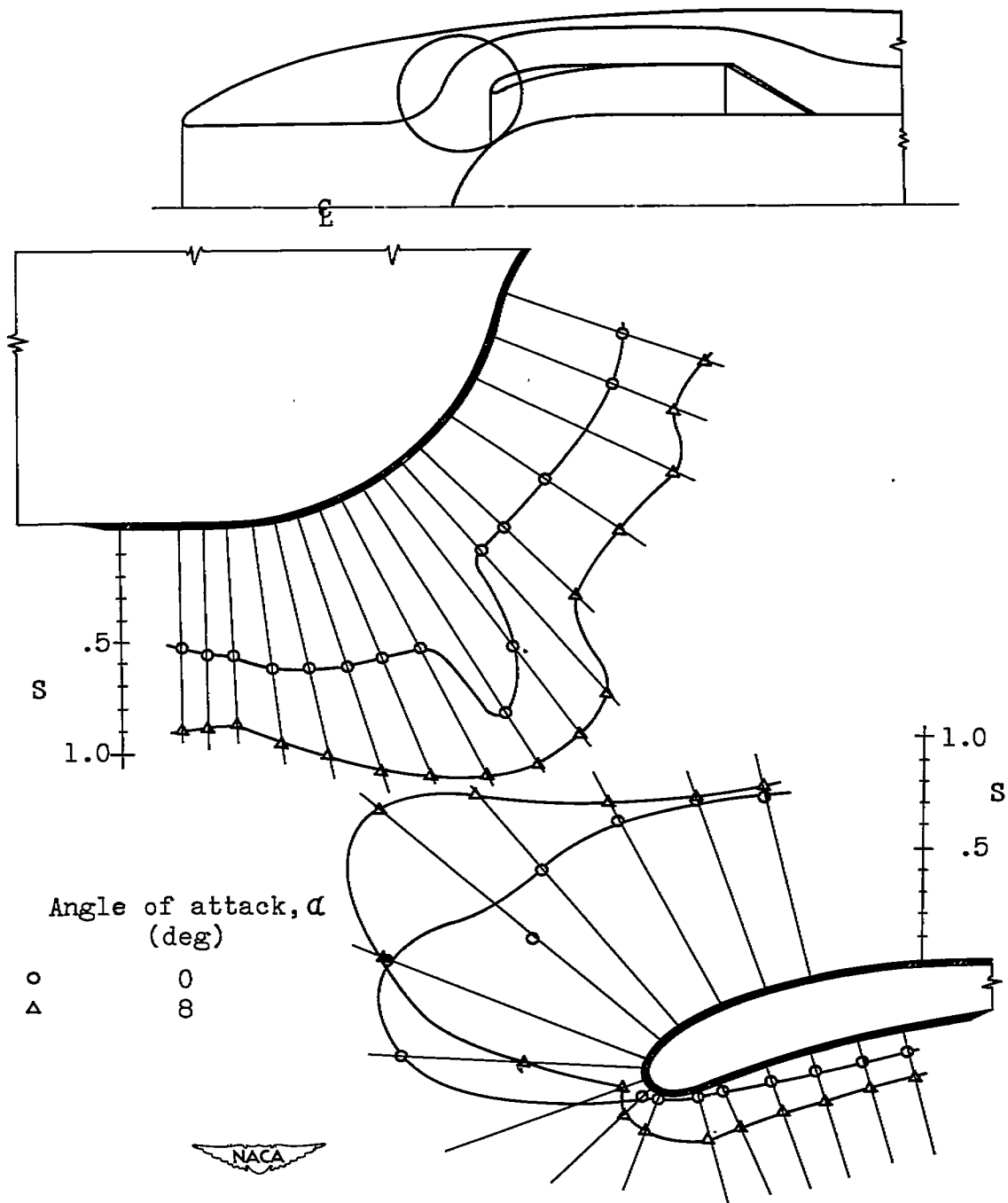


Figure 9.- Continued. Surface pressure distribution at alternate-duct inlet of nose N-1. Main duct blocked; inlet velocity ratio  $V_1/V_0$ , 0.70.



(c) Configuration A-3.

Figure 9.- Concluded. Surface pressure distribution at alternate-duct inlet of nose N-1. Main duct blocked; inlet-velocity ratio  $V_1/V_0$ , 0.70.

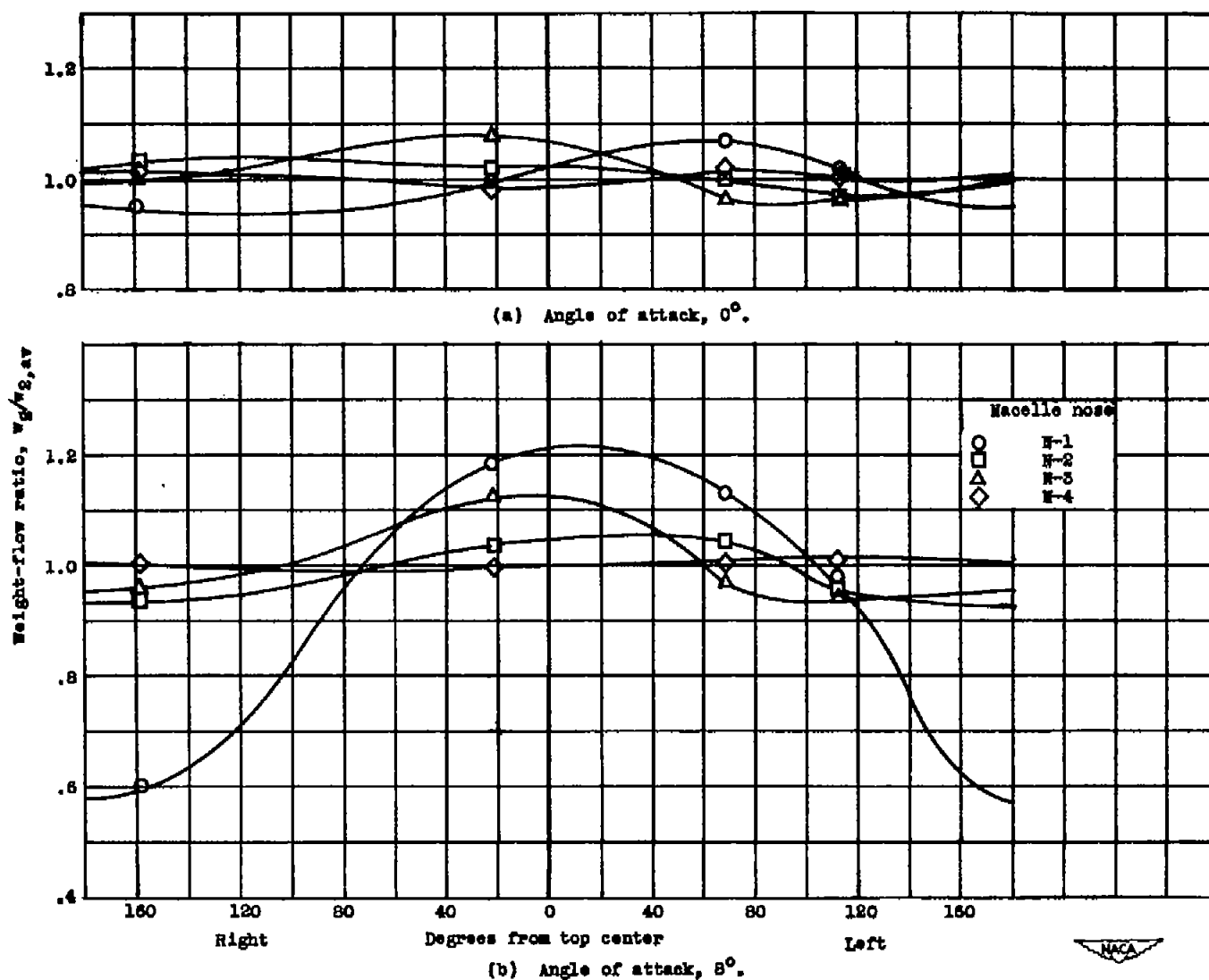


Figure 10.- Circumferential mass-flow variation at compressor inlet for direct-ram installation A-O using several nose-inlet sections. Inlet-velocity ratio  $V_1/V_0$ , design value.

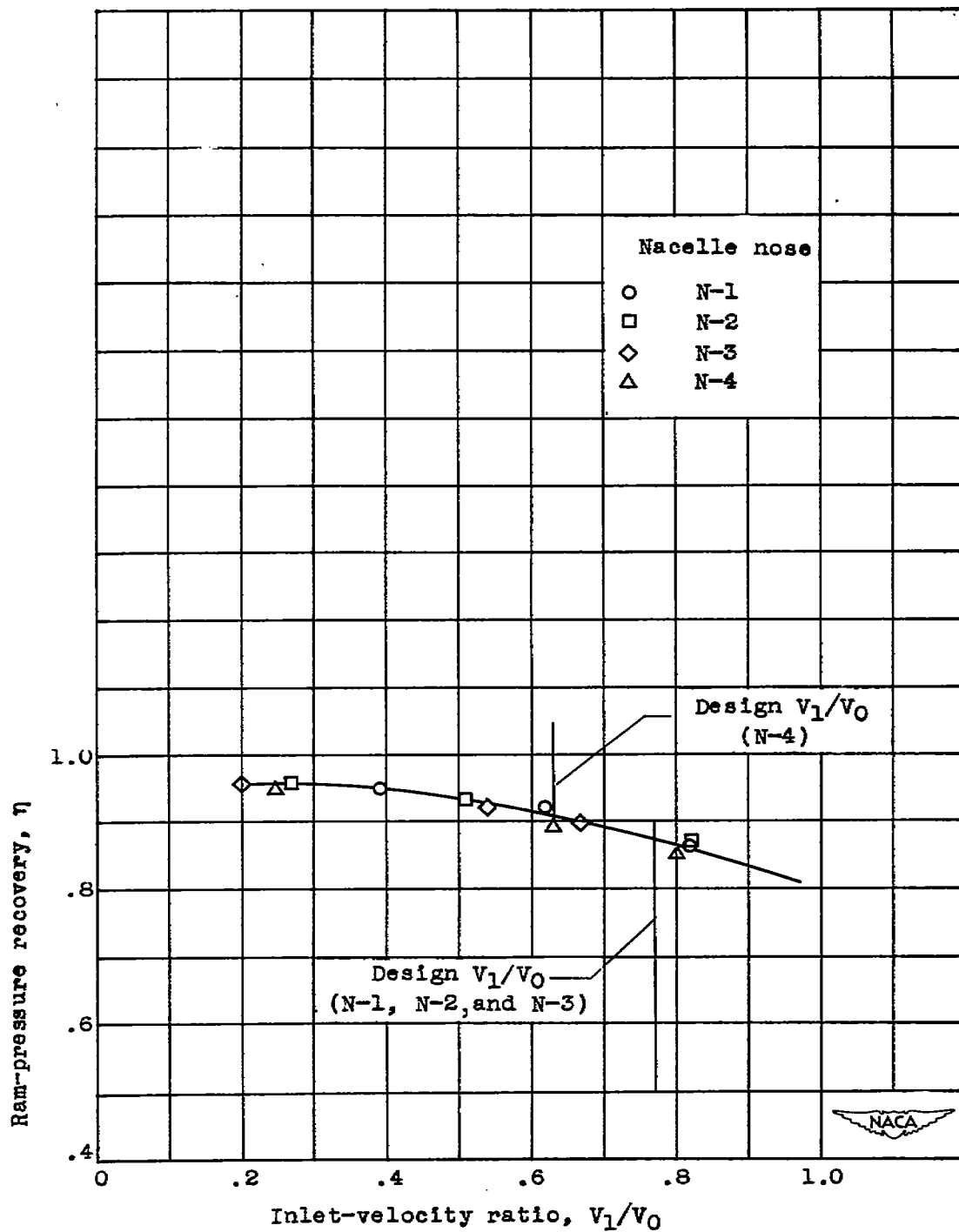


Figure 11.- Variation of ram-pressure recovery with inlet-velocity ratio for direct-ram installation A-O with several nose-inlet sections. Angle of attack  $\alpha$ ,  $0^\circ$ .

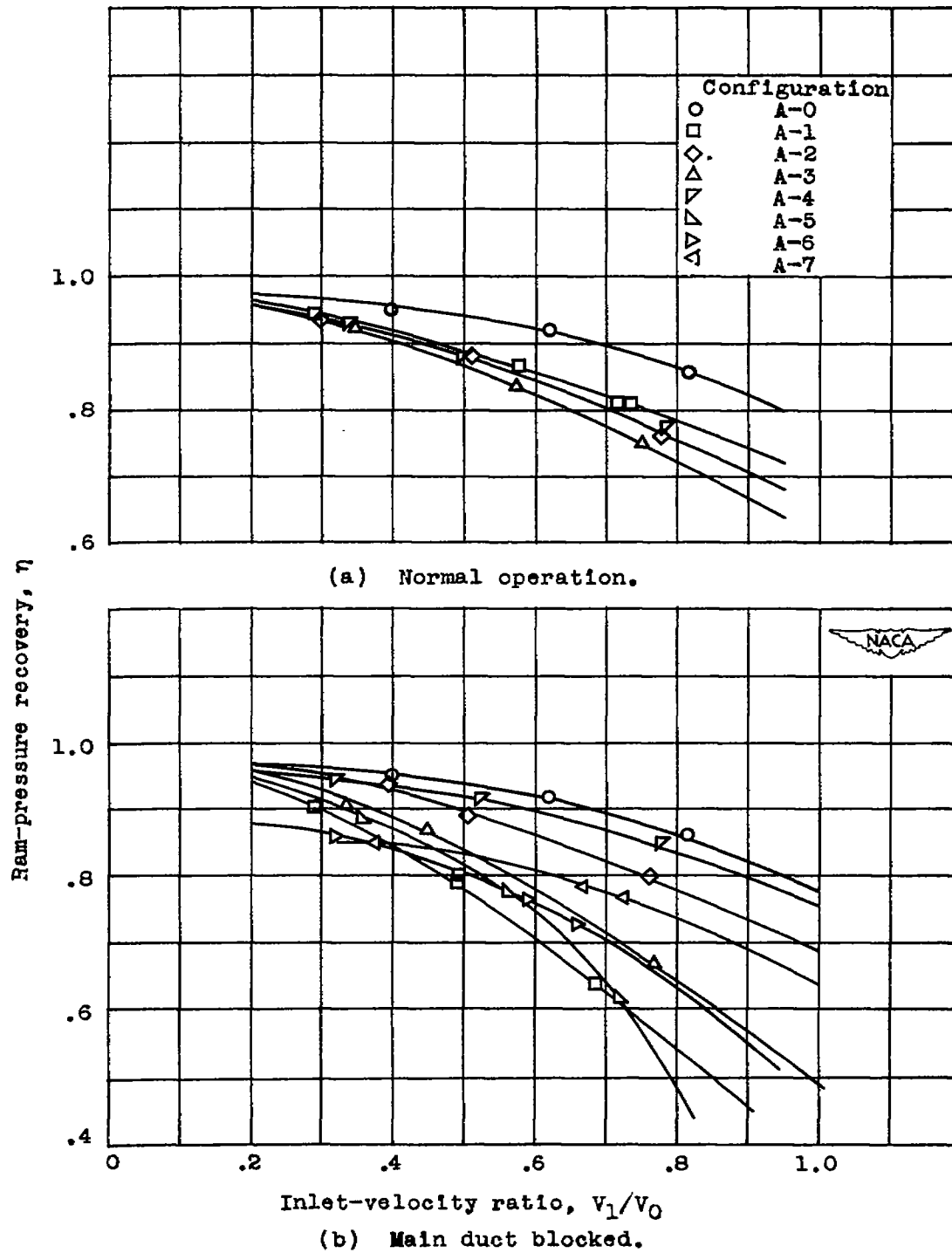
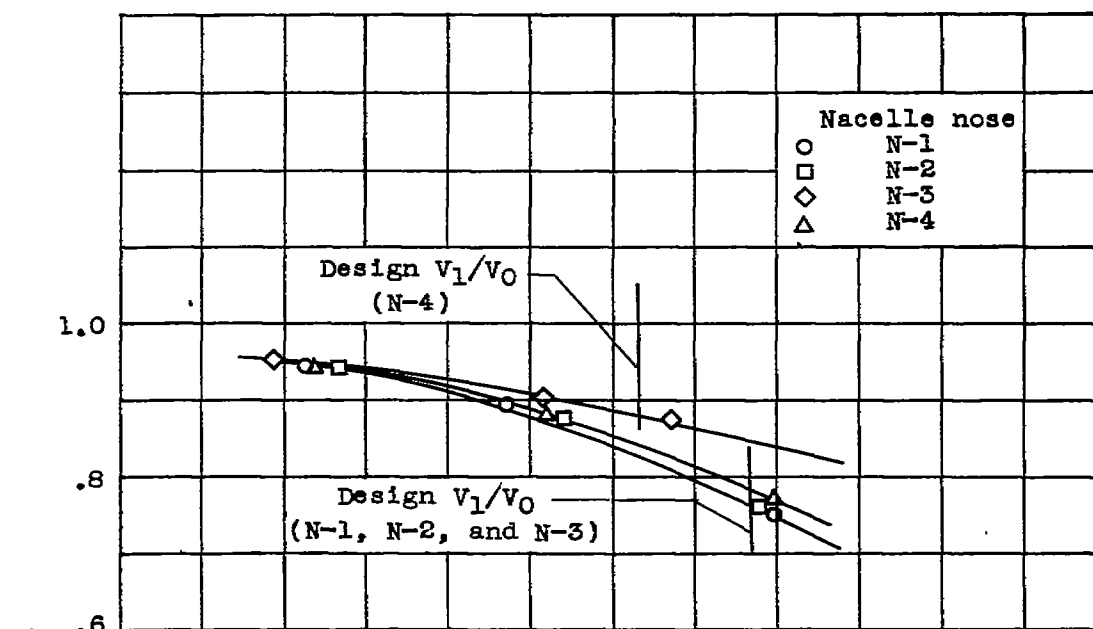
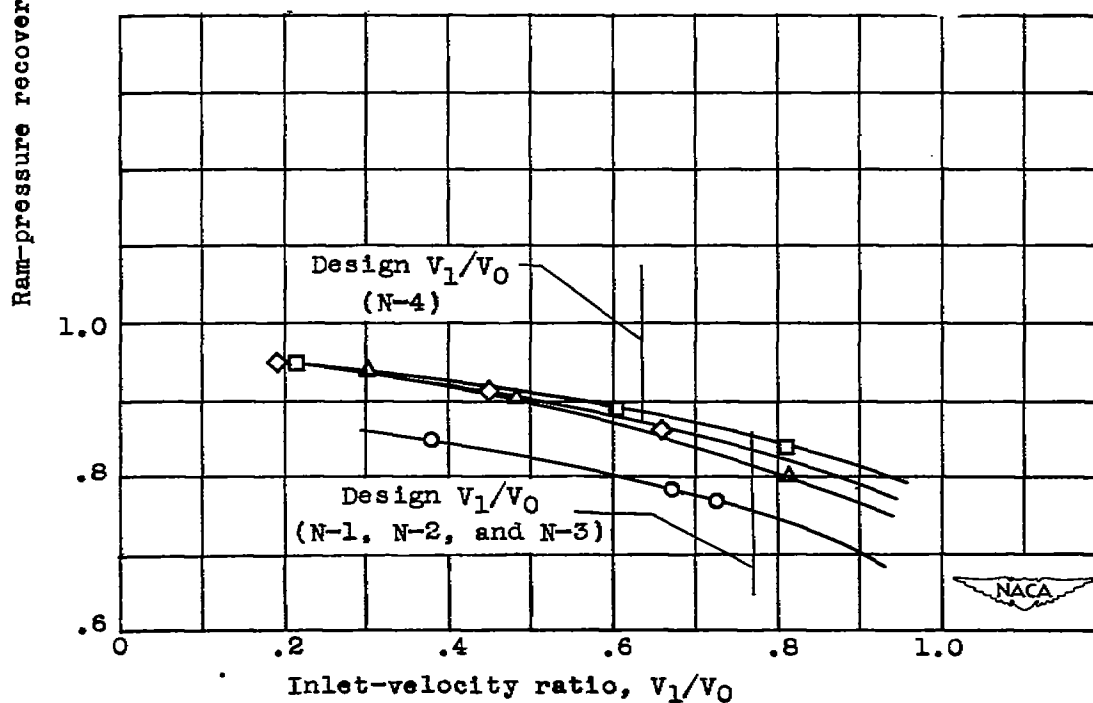


Figure 12.- Variation of ram-pressure recovery with inlet-velocity ratio of nose N-1. Angle of attack  $\alpha$ ,  $0^\circ$ .



(a) Normal operation.



(b) Main duct blocked.

Figure 13.- Variation of ram-pressure recovery with inlet-velocity ratio using configuration A-7 and several nose-inlet sections.



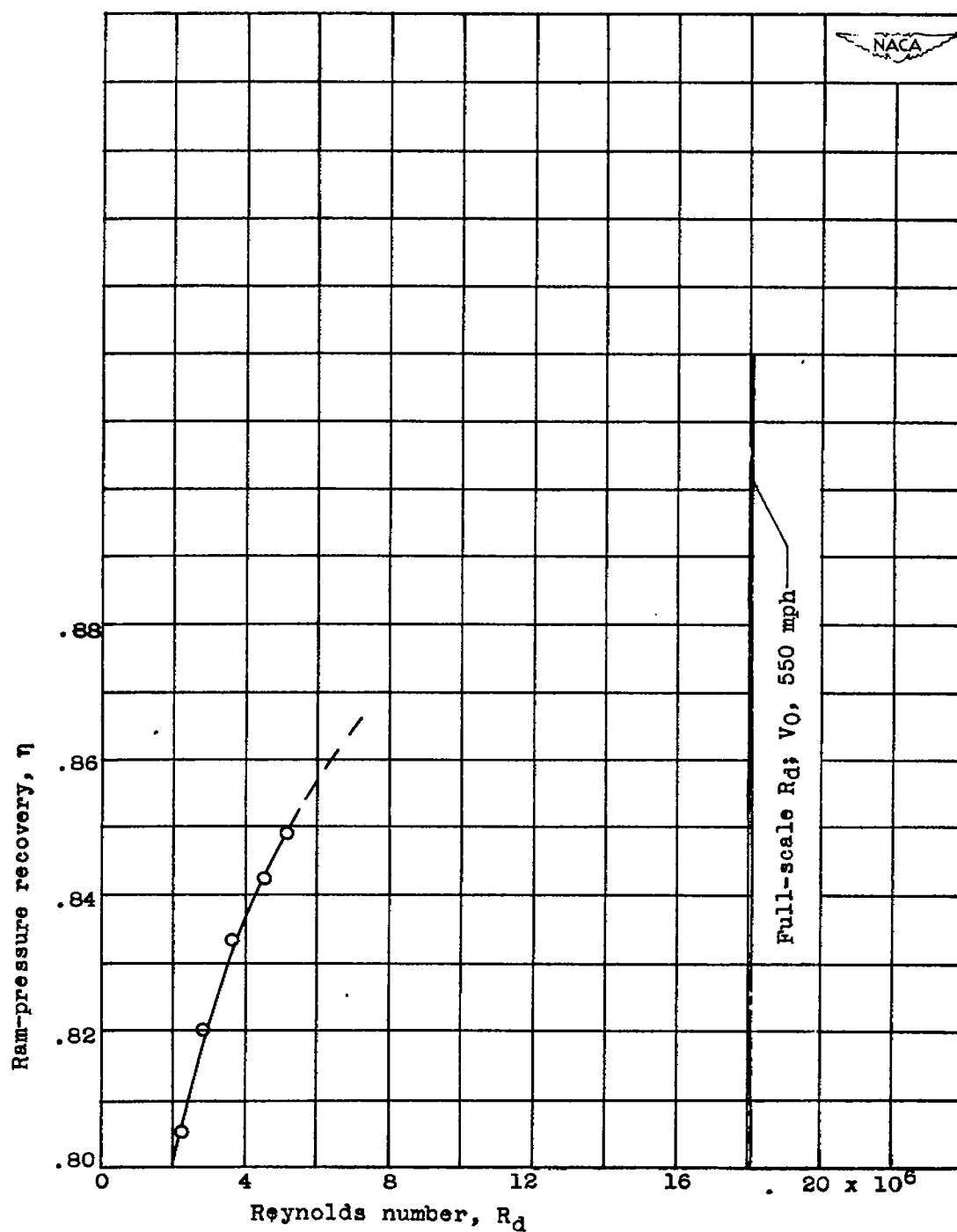


Figure 14.- Variation of ram-pressure recovery with Reynolds number of nose N-1. Configuration A-4; main duct blocked;  $V_1/V_0$ , 0.78.

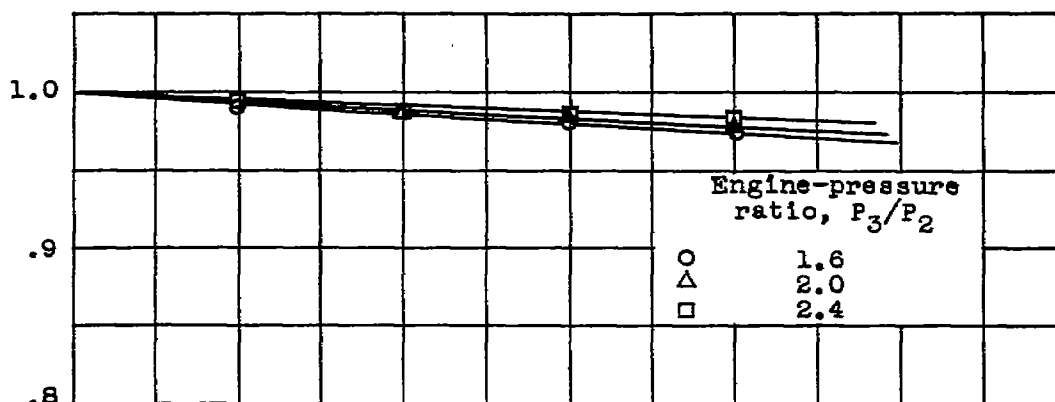
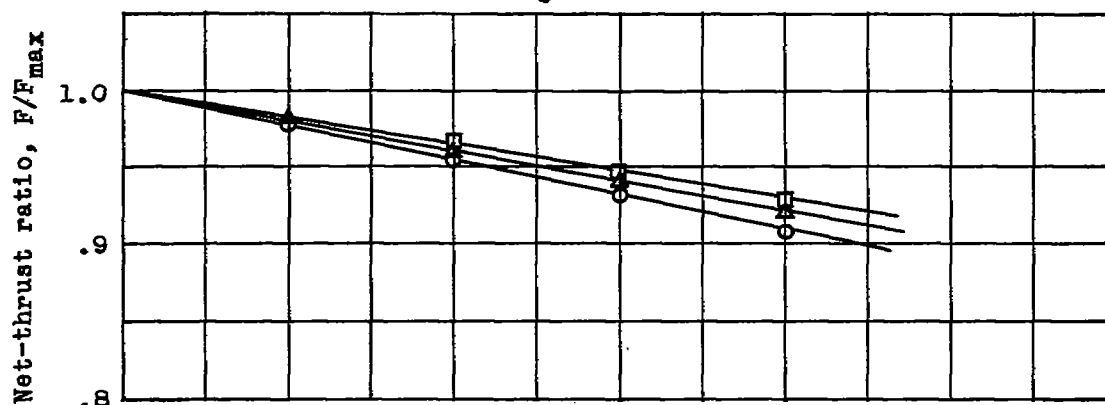
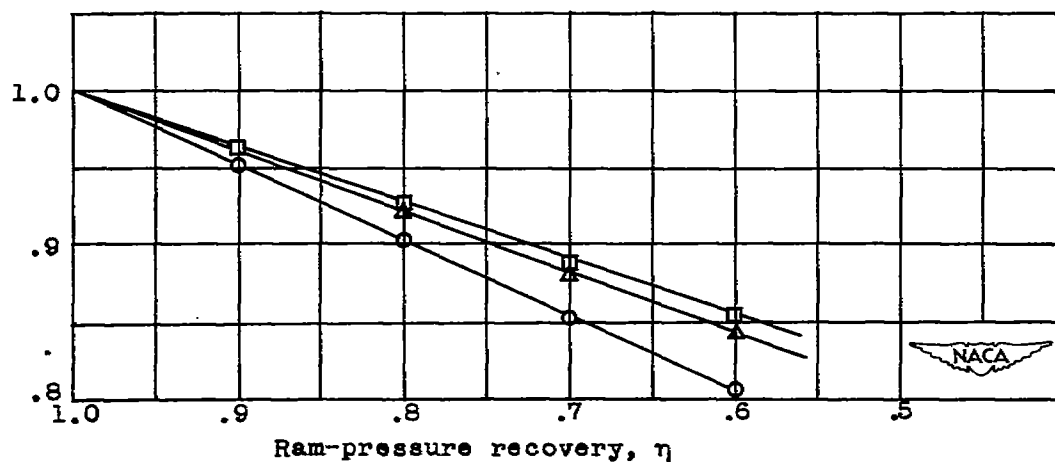
(a)  $M_0, 0.2.$ (b)  $M_0, 0.4.$ (c)  $M_0, 0.6.$ 

Figure 15.- Variation of net-thrust ratio at altitude of 20,000 feet with ram-pressure recovery for several Mach numbers and engine-pressure ratios.

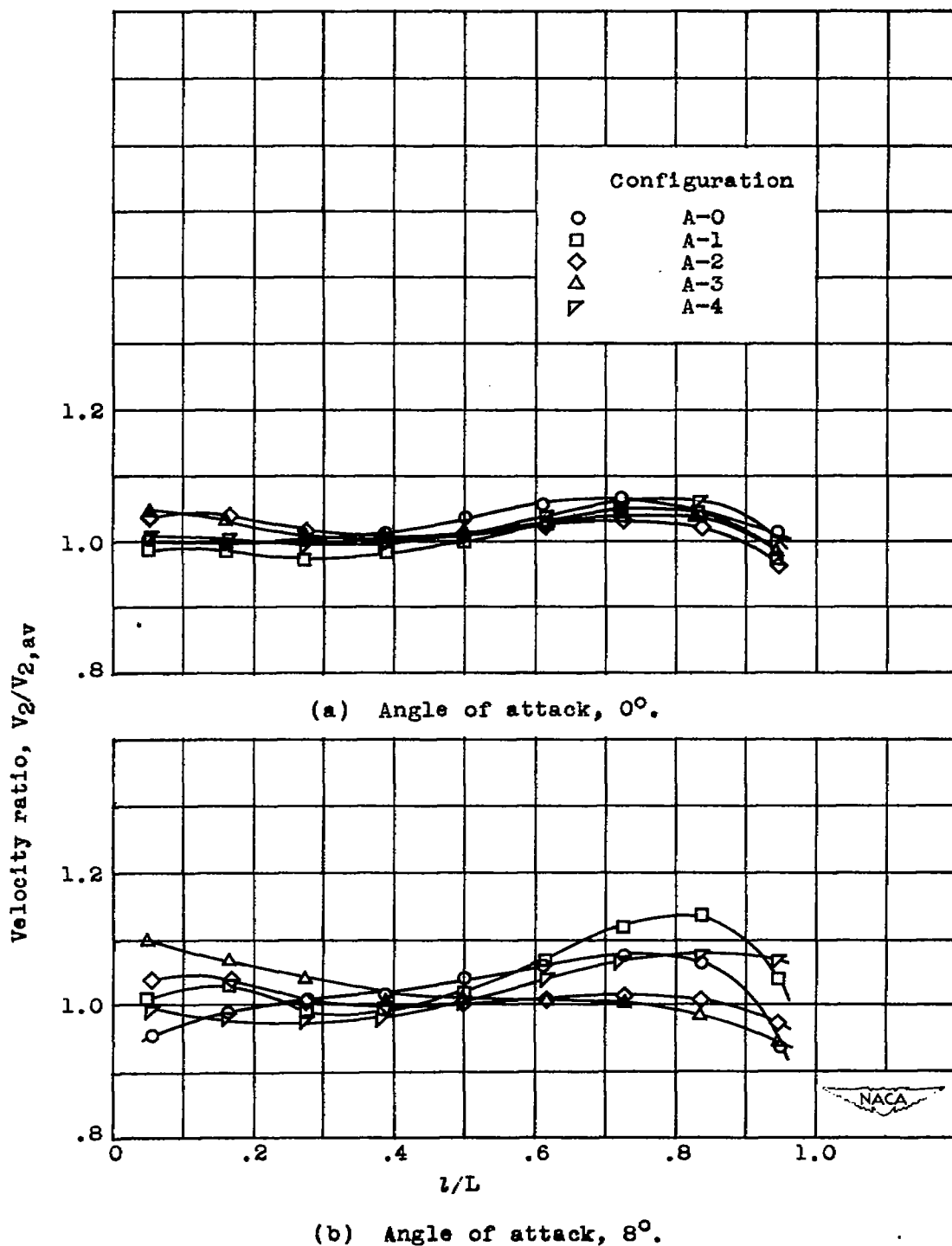


Figure 16.- Typical radial profiles of velocity at compressor inlet of nose N-1. Normal operation;  $V_1/V_0$ , 0.75.

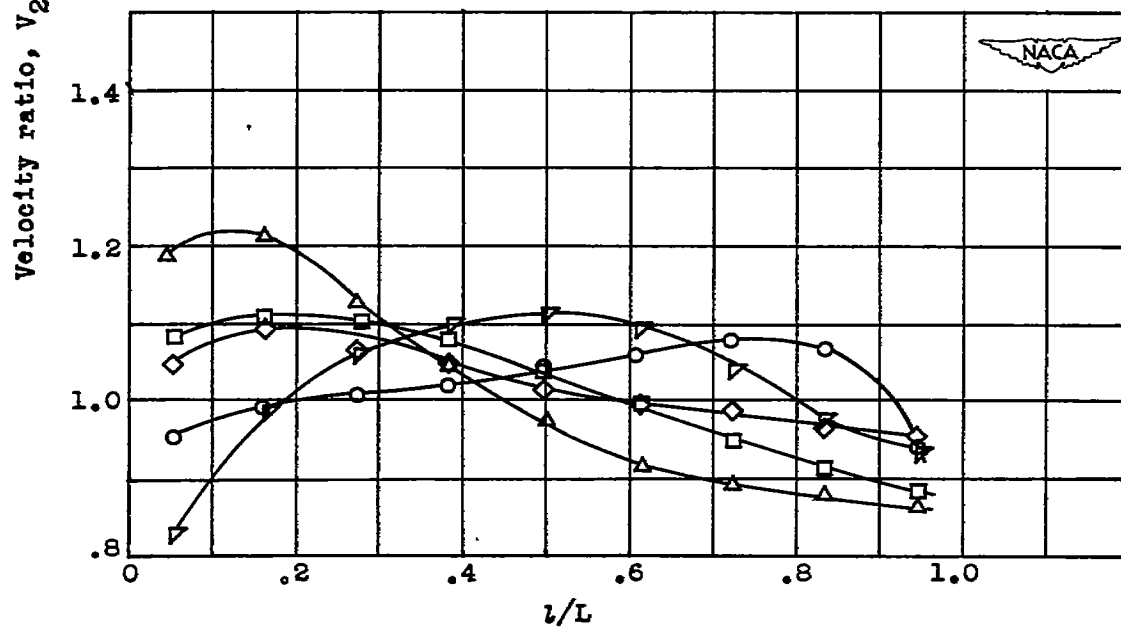
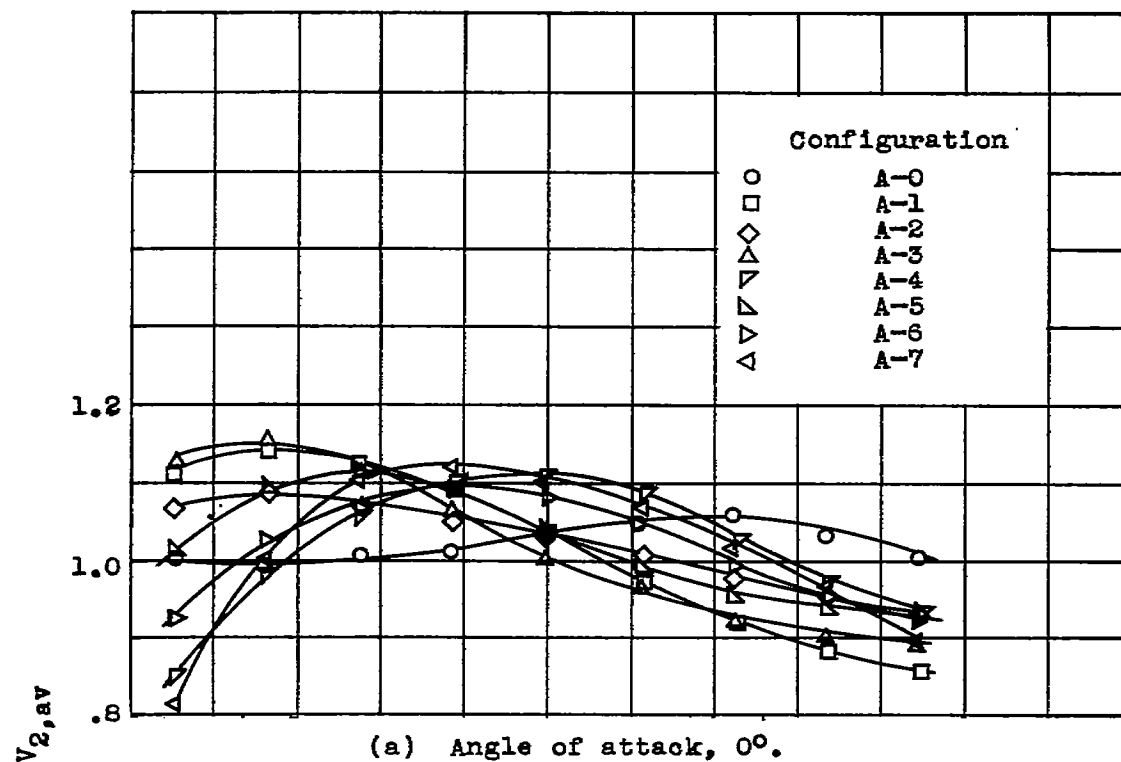
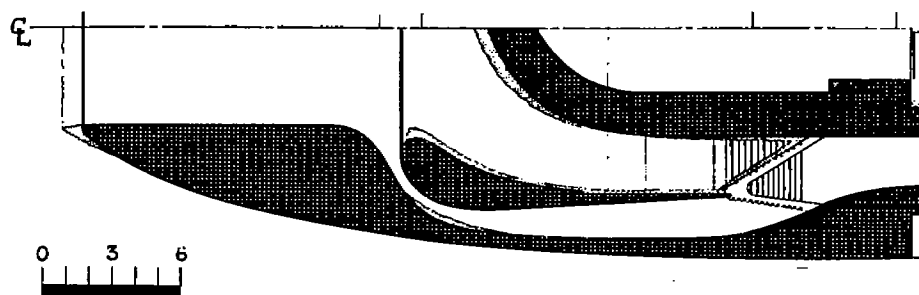
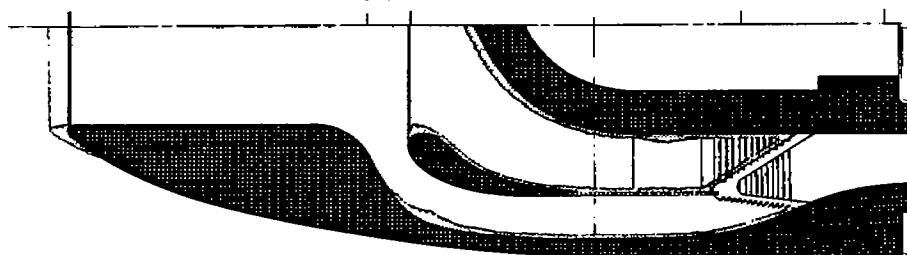


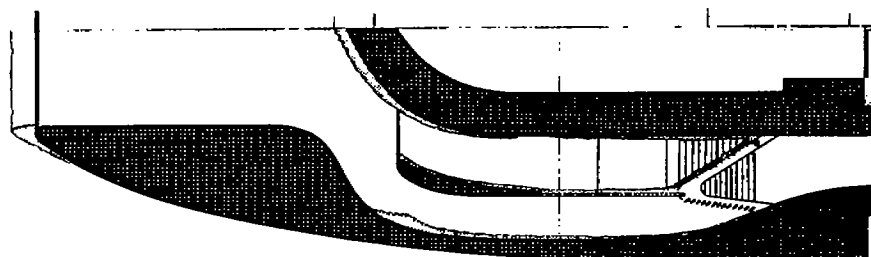
Figure 17.- Typical radial profiles of velocity at compressor inlet of nose N-1. Main duct blocked;  $V_1/V_0$ , 0.75.



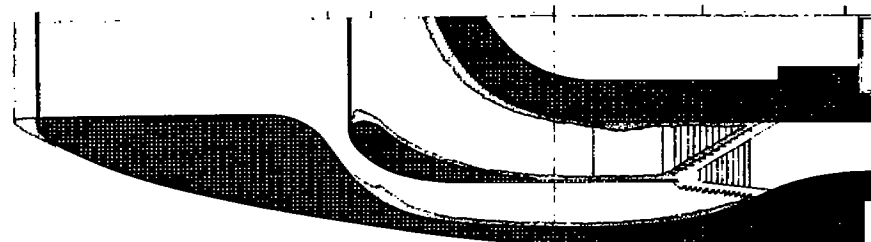
(a) Configuration A-1.



(b) Configuration A-2.



(c) Configuration A-3.

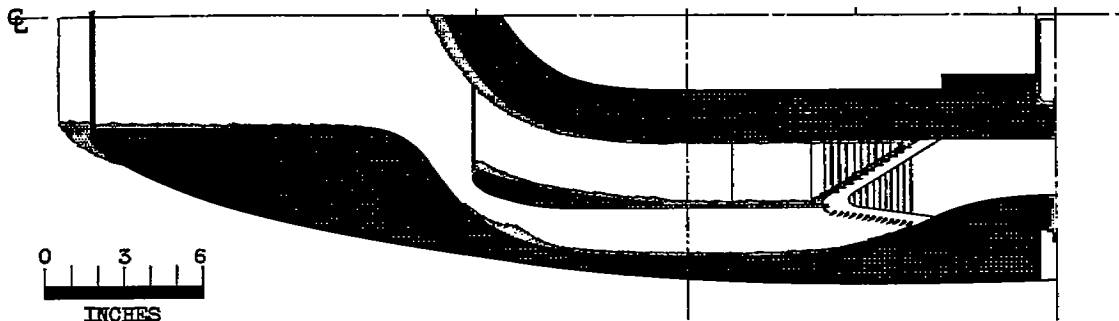


(d) Configuration A-4.

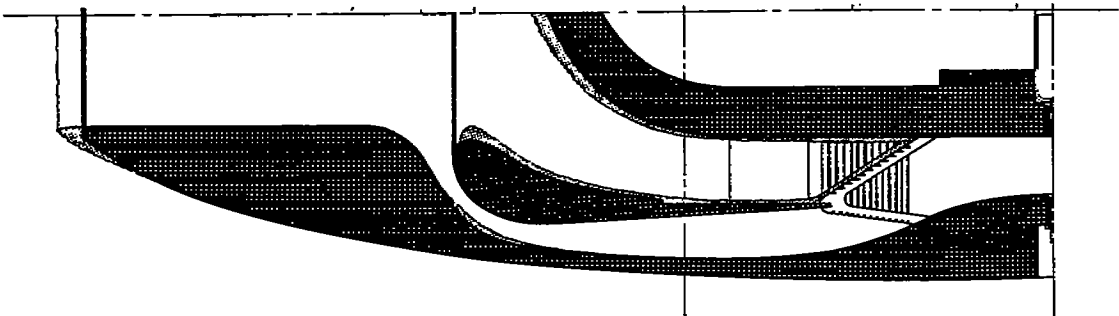


Figure 18. - Cross sections of inlets showing typical ice formations, nose N-1.

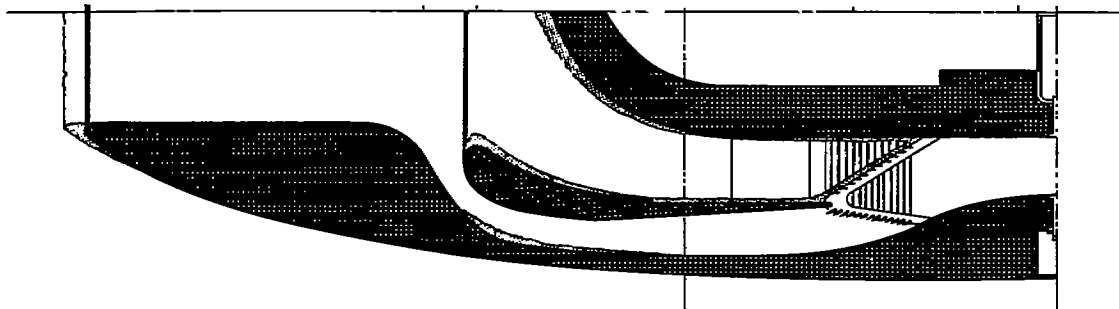
006



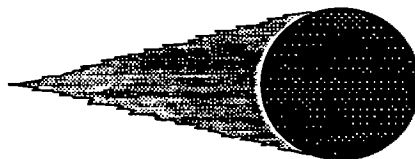
(e) Configuration A-5.



(f) Configuration A-6.



(g) Configuration A-7.

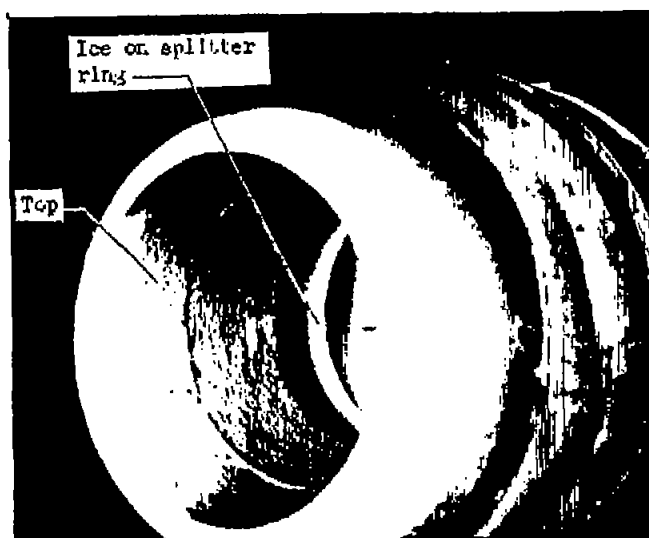


(h) Typical screen ice formation.

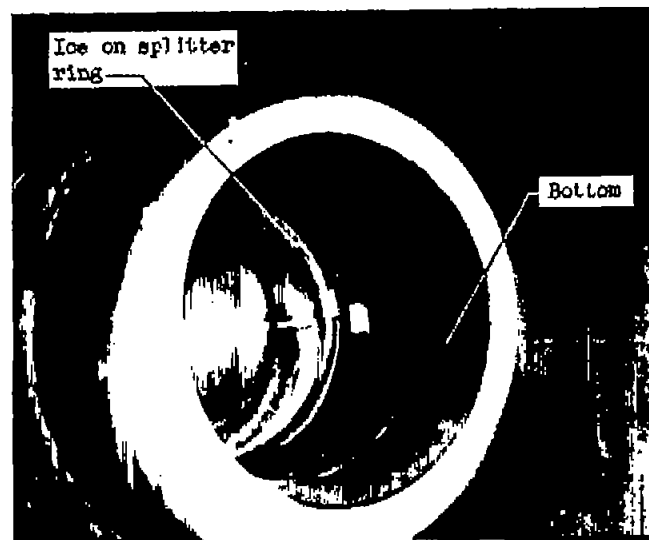


Figure 18. - Concluded. Cross sections of inlets showing typical ice formations, nose N-1.





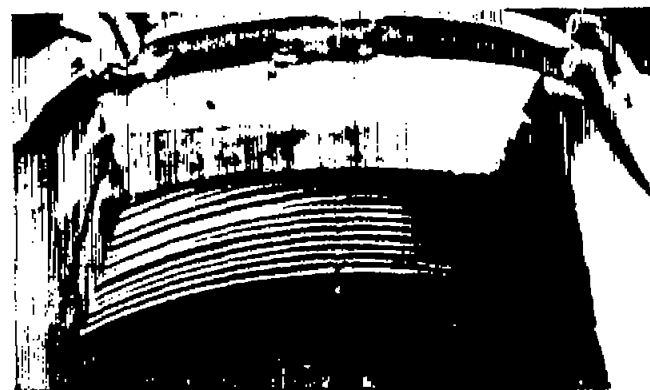
(a) Inlet icing of top quarter of nacelle. Angle of attack,  $8^{\circ}$ .



(b) Inlet icing of bottom quarter of nacelle. Angle of attack,  $8^{\circ}$ .



(c) Icing in alternate duct aft of inlet elbow. Angle of attack,  $0^{\circ}$ .



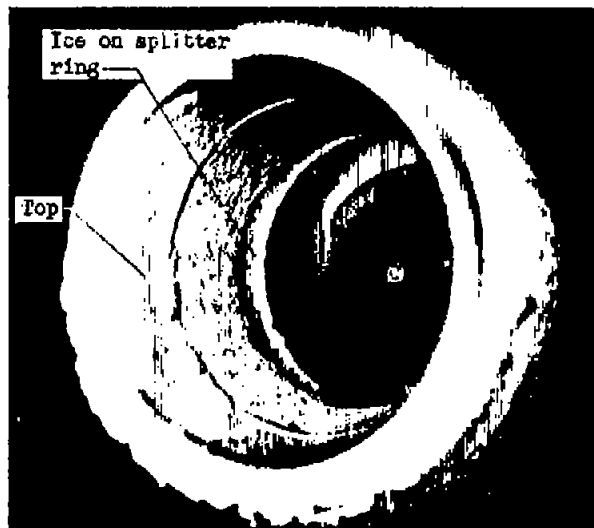
(d) Alternate-duct screen icing. Angle of attack,  $0^{\circ}$ .

NACA  
C-20465  
1-23-48

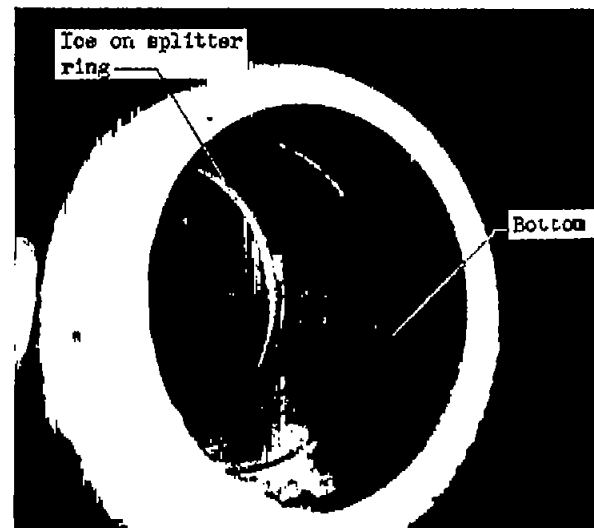
Figure 19. - Typical ice formations on configuration A-2 with nose N-1. Airspeed  $V_0$ , 280 miles per hour; temperature  $T$ ,  $22^{\circ}$  F; icing period, 10 minutes.







(a) Inlet icing of top quarter of nacelle. Angle of attack,  $8^\circ$ .



(b) Inlet icing of bottom quarter of nacelle. Angle of attack,  $8^\circ$ .



(c) Icing on alternate-dust inspection door and heavy ridges of ice on modeling clay fairing. Angle of attack,  $0^\circ$ .



(d) Icing of alternate-dust screen. Angle of attack,  $0^\circ$ .

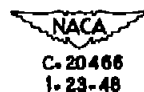
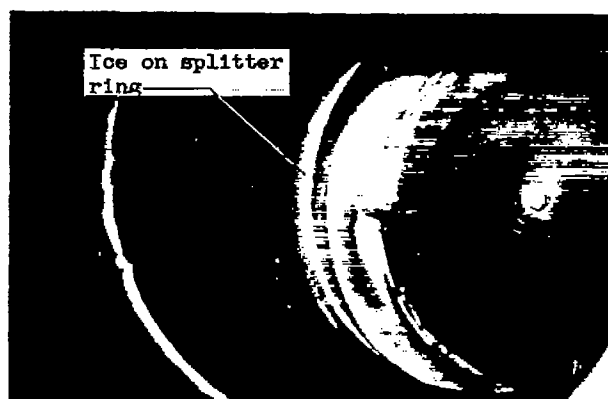
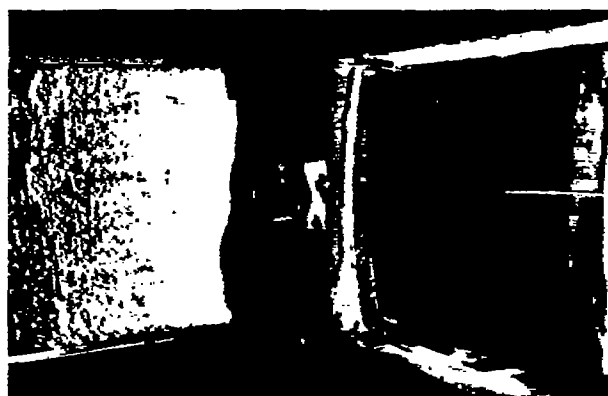


Figure 20. - Ice formations on configuration A-4 with nose N-1. Airspeed  $V_0$ , 280 miles per hour; temperature  $T$ ,  $20^\circ$  F; icing period, 10 minutes.

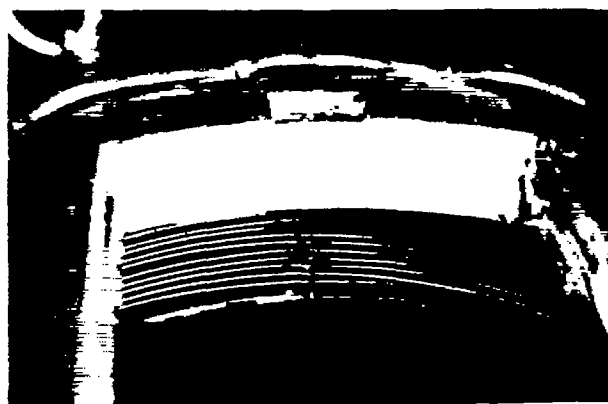




(a) Ice formation on alternate inlet.



(b) Icing of alternate-duct inspection door.



(c) Icing of alternate-duct screen.

NACA  
C-20467  
1-23-47

Figure 21. - Typical ice formations on configuration A-7 with nose N-1. Airspeed  $V_0$ , 260 miles per hour; temperature  $T$ ,  $20^\circ$  F; icing period, 10 minutes; angle of attack,  $\alpha$ ,  $0^\circ$ .



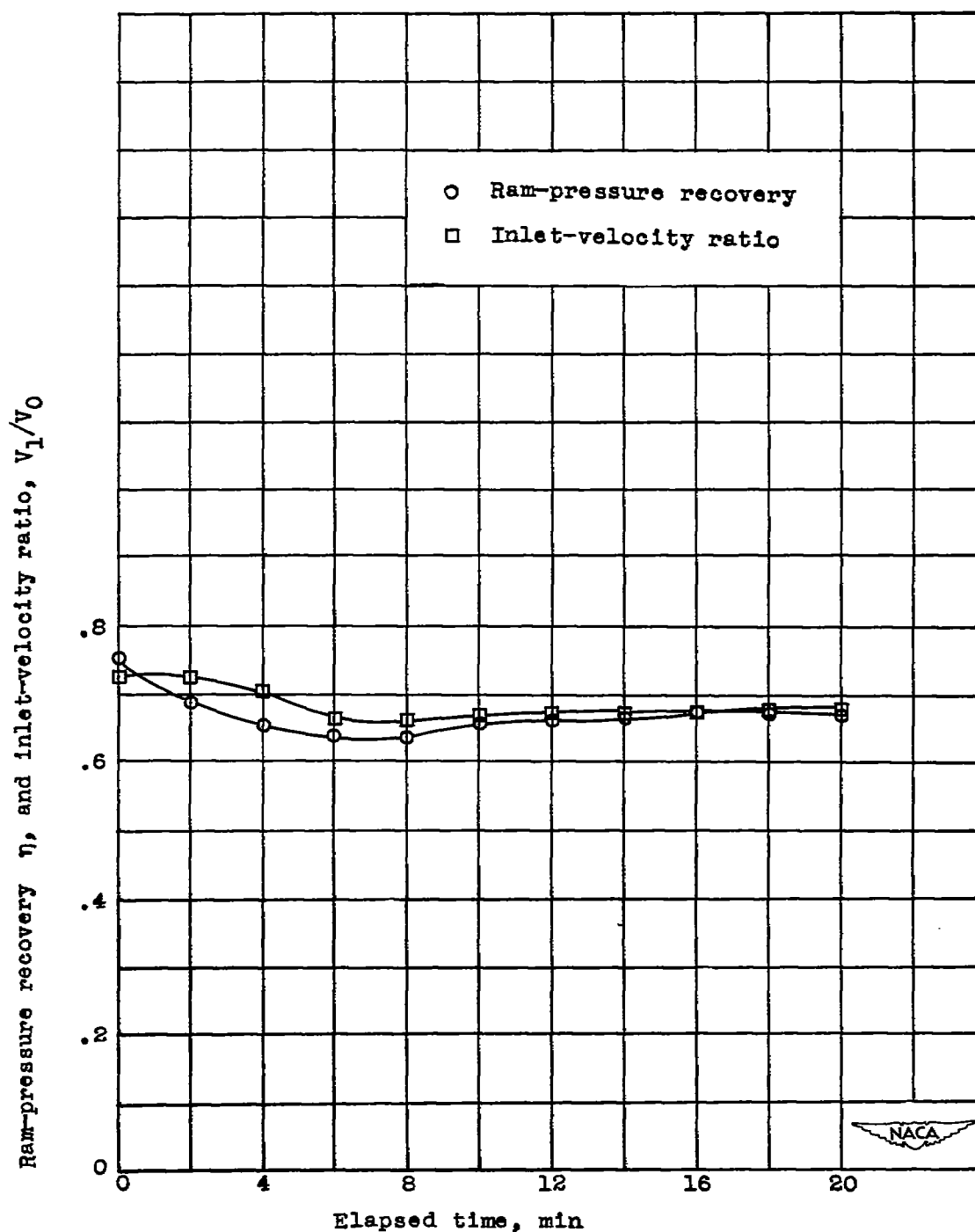
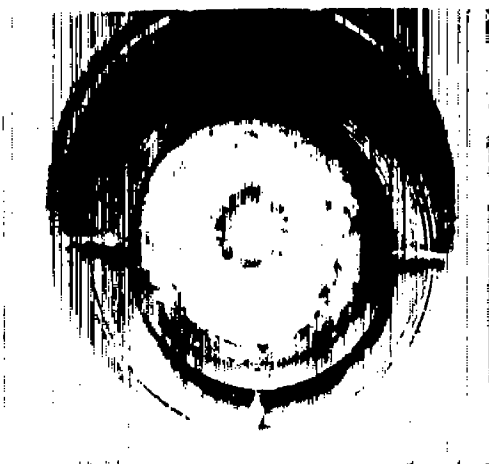
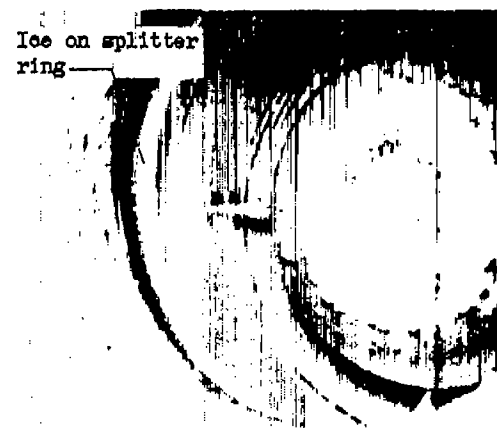


Figure 22.- Change in ram-pressure recovery and inlet-velocity ratio in heavy icing condition for configuration A-7 of nose N-1. Both ducts open at start and screens in place; airspeed  $V_0$ , 280 miles per hour; angle of attack  $\alpha$ ,  $0^\circ$ .





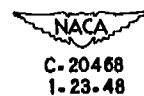
(a) Icing of main-duct screen.



(b) Icing of alternate inlet.



(c) Ice formation in alternate-duct elbow and on inspection door.



(d) Icing on alternate-duct screen.

Figure 23. - Ice formations on configuration A-7 with nose N-1. Both ducts open; airspeed  $V_0$ , 260 miles per hour; temperature  $T$ ,  $20^\circ$  F; icing period, 20 minutes; angle of attack  $\alpha$ ,  $0^\circ$ .





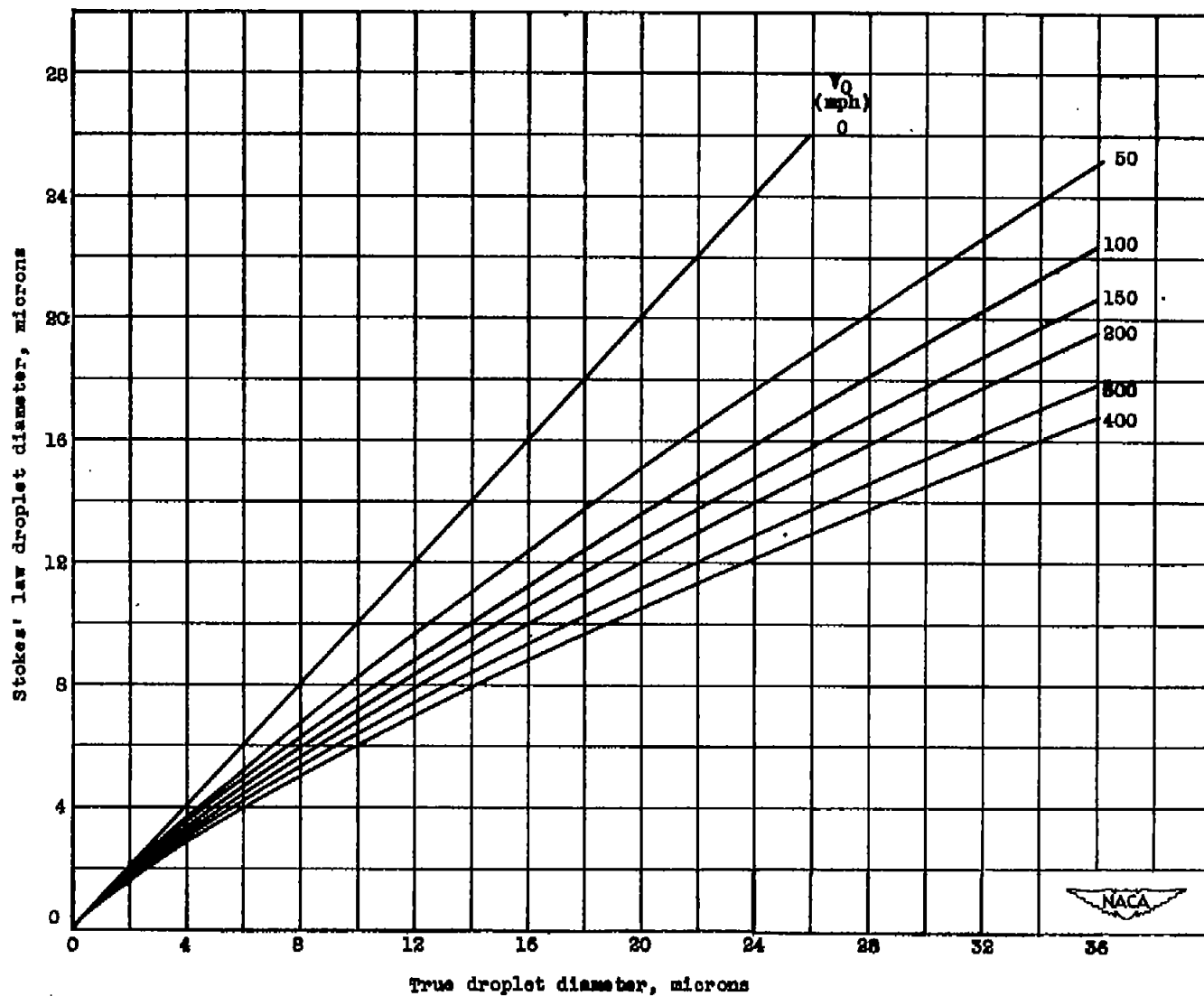


Figure 24. - Variation of droplet size with velocity.

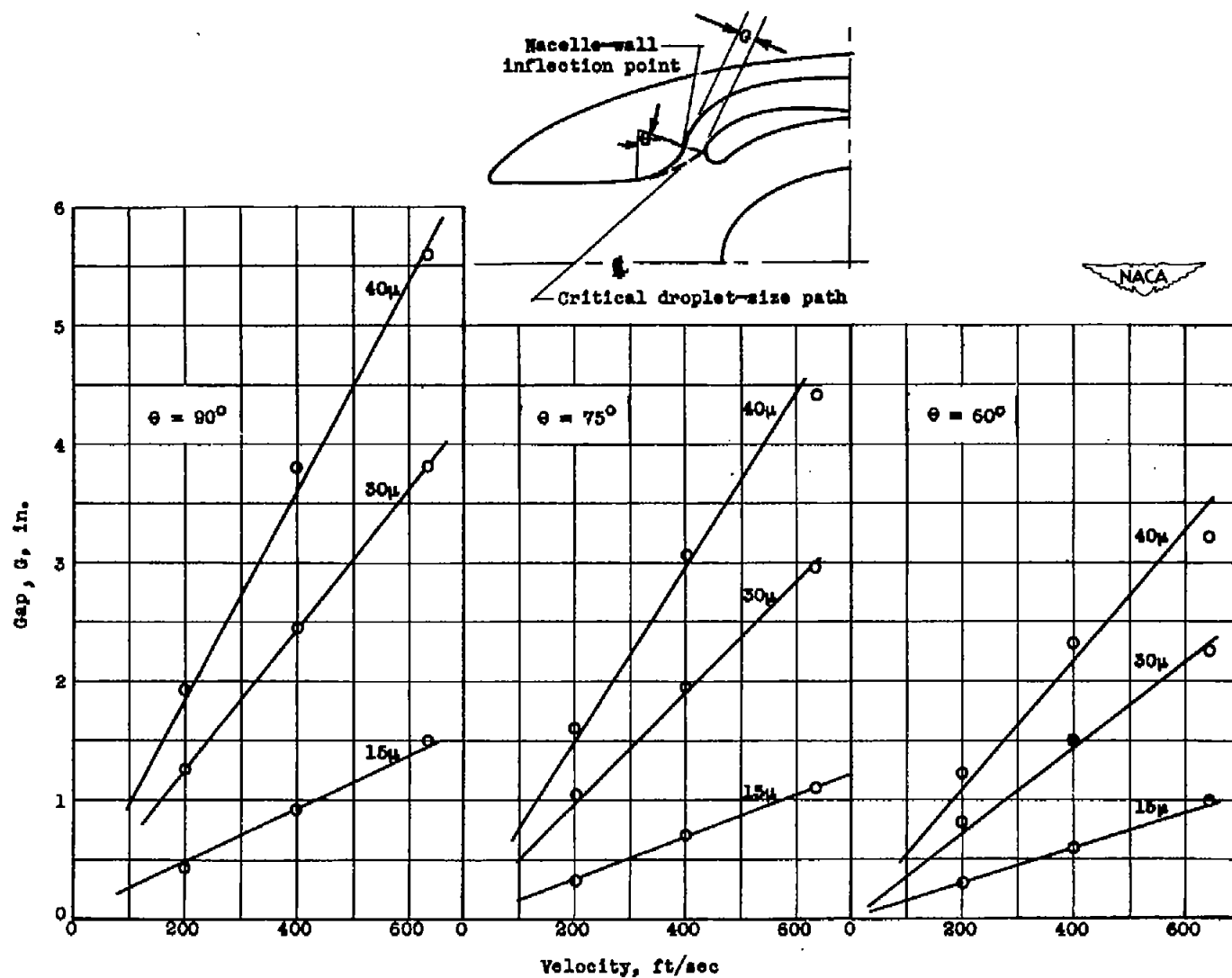


Figure 25.- Variation of gap with velocity for various values of alternate-inlet turning angle  $\Theta$  and critical droplet size.

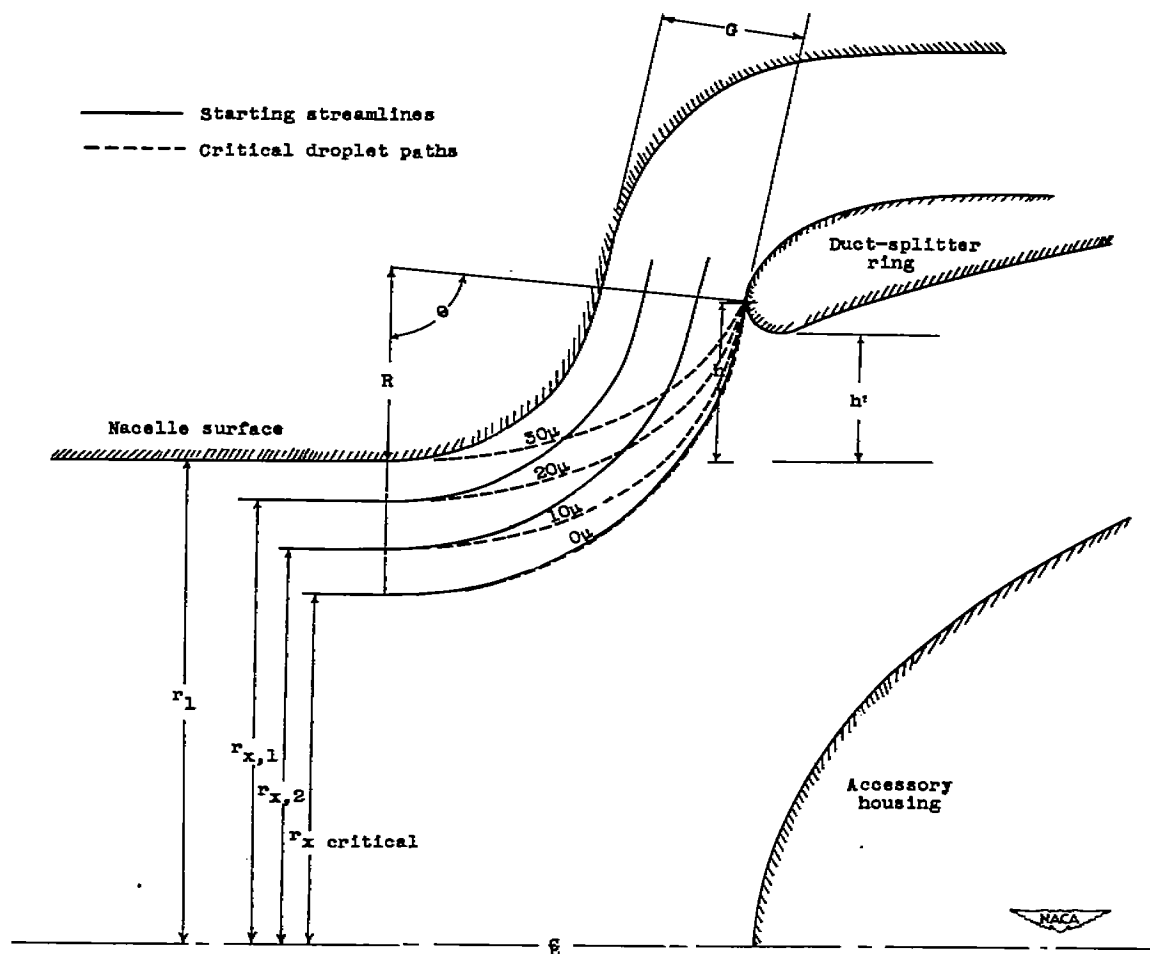


Figure 26. - Effect of starting streamlines on critical droplet size entering alternate-duct inlet.

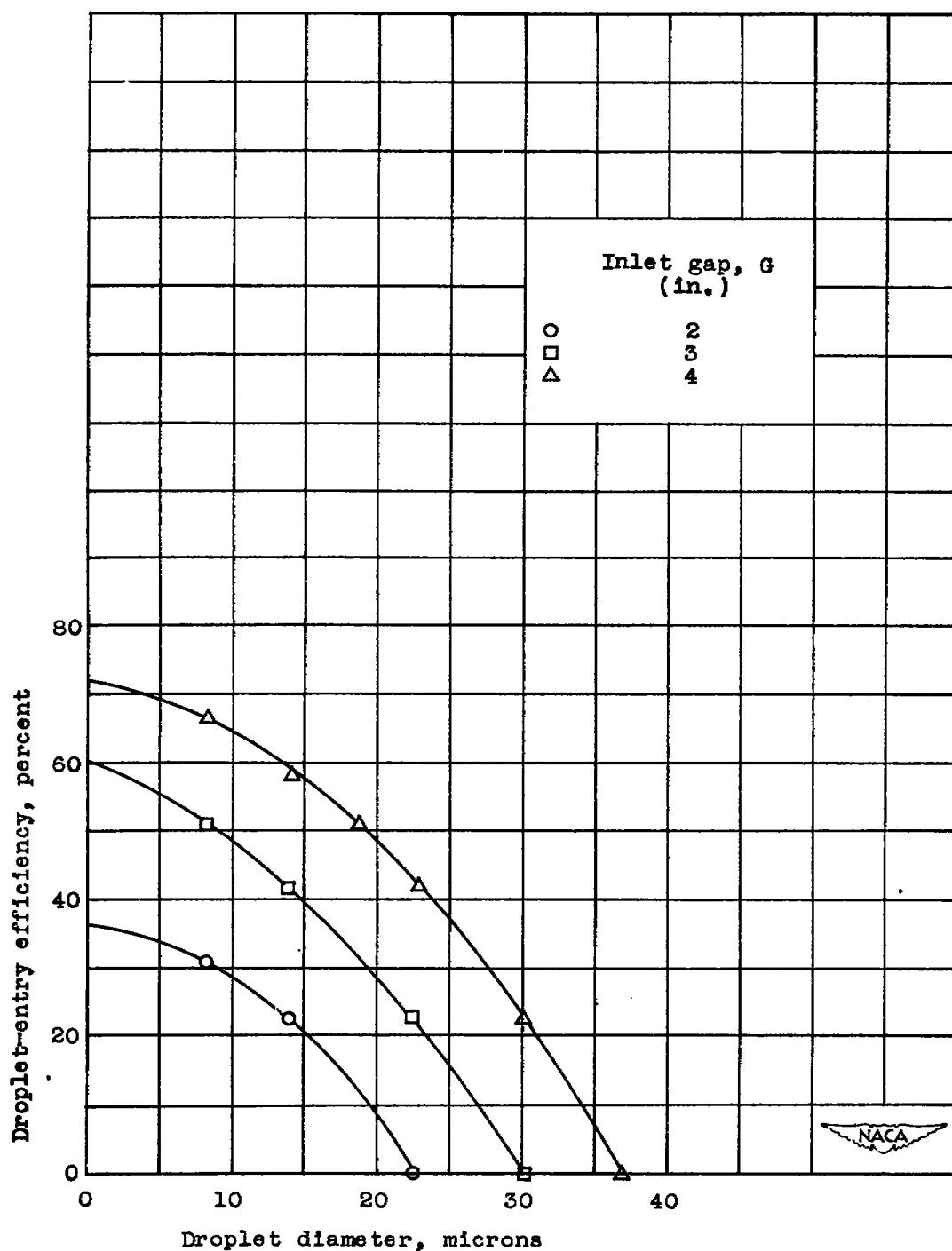


Figure 27.- Percentage of various sized droplets entering alternate-duct inlet. Airspeed at nacelle inlet  $V_1$ , 435 miles per hour; alternate-inlet turning angle  $\theta$ ,  $75^\circ$ ; nacelle-inlet radius  $r_1$ , 8.4 inches; alternate-duct inlet turning radius  $R$ , 4.0 inches.

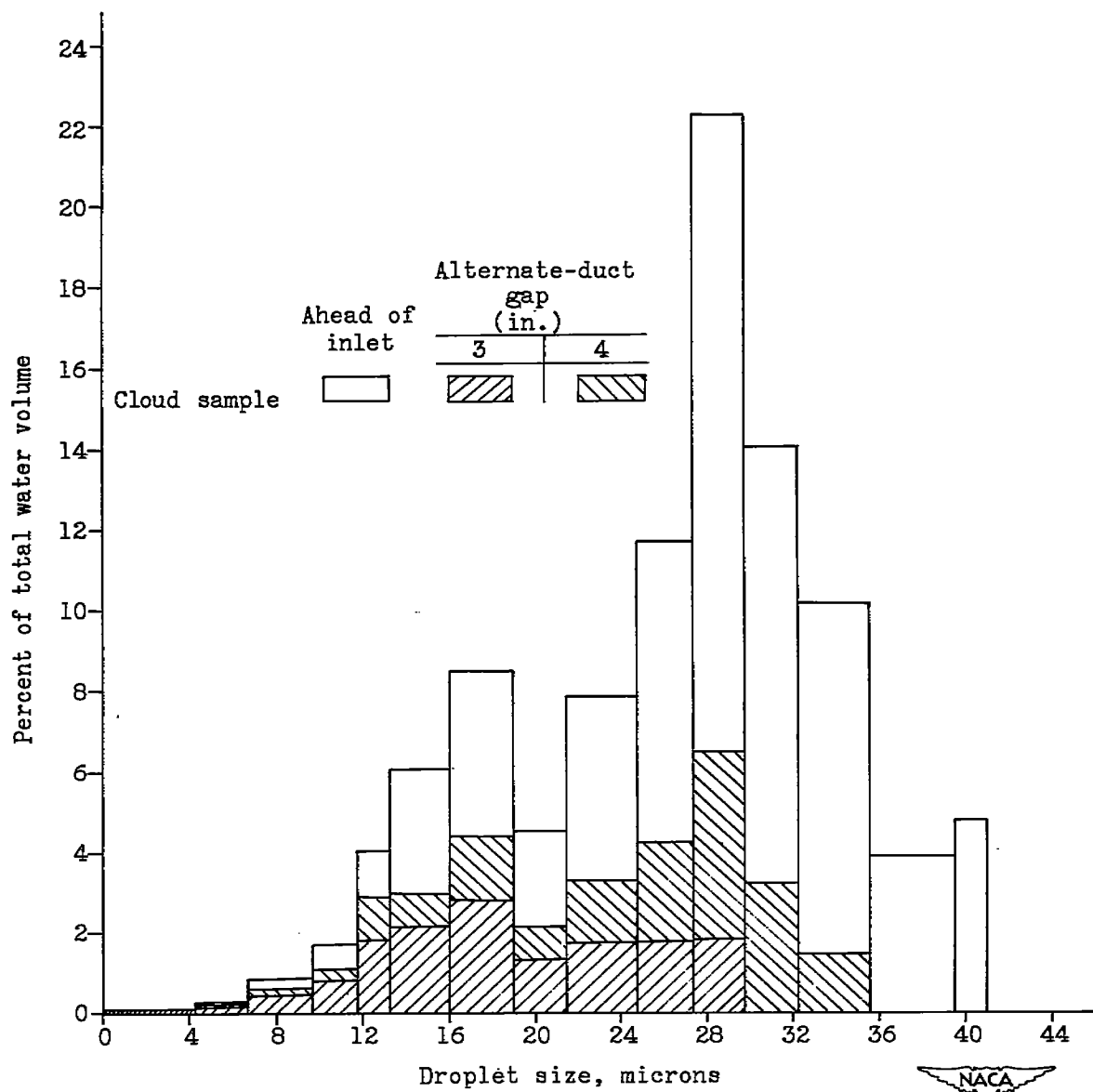


Figure 28.- Effect of inlet-gap size on volume of water intake at alternate-duct inlet for typical cloud sample.